Geostatistical Inversion for Subsurface Characterization Using Stein Variational Gradient Descent with Autoencoder Neural Network: An Application to Geologic Carbon Sequestration

Mingliang Liu[1], **Dario Grana**[2] and **Tapan Mukerji**[1,3]

[1] Department of Energy Science and Engineering, Stanford University, USA.

[2] Department of Geology and Geophysics, University of Wyoming, USA.

[3] Department of Geophysics and Department of Earth & Planetary Science, Stanford University, USA.

Corresponding author: Mingliang Liu (mliu9@stanford.edu)

Key Points:

- A geostatistical inversion method is developed by integrating Stein variational gradient descent with autoencoder.
- The developed method provides an efficient approach for accurate subsurface characterization with uncertainty quantification.
- An integrated reservoir characterization of the Mount Simon Sandstone at the Illinois Basin - Decatur Project is presented.

ABSTRACT

Geophysical subsurface characterization plays a key role in the success of geologic carbon sequestration (GCS). While deterministic inversion methods are commonly used due to their computational efficiency, they often fail to adequately quantify the model uncertainty, which is essential for informed decision-making and risk mitigation in GCS projects. In this study, we propose the SVGD-AE method, a novel geostatistical inversion approach that integrates geophysical data with prior geological knowledge to estimate subsurface properties. SVGD-AE combines Stein Variational Gradient Descent (SVGD) for sampling high-dimensional distributions with an autoencoder (AE) neural network for re-parameterizing reservoir models, aiming to accurately preserve geostatistical characteristics of reservoir models derived from geological priors. Through two synthetic examples, we demonstrate that the SVGD-AE method outperforms traditional probabilistic methods, particularly in inverse problems with complex posterior distributions. Then, we apply SVGD-AE to the Illinois Basin - Decatur Project (IBDP), a large-scale CO_2 storage initiative in Decatur, Illinois, USA. The resulting petrophysical models with quantified uncertainty enhance our understanding of subsurface properties and have broad implications for the feasibility, decision making, and long-term safety of CO_2 storage at the IBDP.

Plain Language Summary

Geologic carbon sequestration (GCS) provides a promising solution to mitigate the adverse effects of human-generated CO_2 emissions on the climate. GCS involves capturing CO_2 emitted from industrial activities, such as those from coal-fired power plants, and storing it deep underground. This procedure effectively prevents gas from entering the atmosphere and contributing to global warming. To ensure the success and safety of GCS projects, it is crucial to have a comprehensive understanding of the subsurface, including rock and fluid properties. In this research, we present an innovative probabilistic approach for quantifying subsurface properties using geophysical data. The proposed methodology has been successfully applied to the Illinois Basin - Decatur Project (IBDP), which is a large-scale CO_2 storage initiative in Decatur, Illinois, USA. Our study enhances the comprehension of subsurface attributes and supports informed decision-making regarding the long-term safety of CO_2 storage at the IBDP.

1. Introduction

The ever-growing global demand for energy, combined with increasing environmental concerns regarding greenhouse gas emissions, has led to a surge in the development and implementation of sustainable energy technologies. Among these solutions, geologic carbon sequestration (GCS) has emerged as a promising approach to alleviate the impact of human-induced carbon dioxide (CO_2) emissions on the climate (Metz et al., 2005). GCS involves capturing CO_2 from industrial sources, such as coal-fired power plants, and injecting it deep into geological formations. This procedure effectively prevents large-scale CO_2 emissions into the atmosphere, thereby reducing its contribution to global warming. However, the success and safety of GCS projects critically depends on a profound understanding of the subsurface geological characteristics and processes, which is generally referred to as *subsurface characterization* (Grana et al., 2022).

Geophysical inversion is a widely used technique that leverages indirect measurements, including seismic, electromagnetic and gravity surveys, to infer the properties of subsurface rock and fluid, such as porosity, permeability and saturation (Davis et al., 2019; Wang H. et al., 2020; Zhao L. et al., 2021; Huang, 2022). Geophysical inversion methods can be broadly classified into two groups: deterministic and probabilistic methods (Tarantola, 2005). Deterministic methods have gained widespread applications in practice due to their speed and efficiency. They aim to find the optimal model, typically a local optimal and the simplest (yet often overly smoothed) model, that is consistent with the observed data (Aster et al., 2018). However, practical challenges such as limited and noisy data as well as imperfect forward models, introduce uncertainties that lead to multiple possible solutions (i.e., non-uniqueness). In this perspective, deterministic approaches are unable to quantify such uncertainties adequately.

In contrast to deterministic methods, probabilistic inversion methods model the solution as a probability density function (PDF), enabling a thorough assessment of uncertainty associated with the model parameters (Tarantola, 2005). This information about uncertainty holds great significance in various aspects of GCS projects. For instance, it plays a crucial role in storage capacity estimation for site characterization before injection, as well as in well planning and geophysical data acquisition during the injection period. By adopting probabilistic inversion, GCS endeavors can better account for and manage the inherent uncertainties, leading to more reliable and informed decision-making processes (Scheidt et al., 2018).

In probabilistic approaches to geophysical inversion problems, the prior PDF of model parameters is modeled from the geological knowledge of the study area. This prior PDF is then updated through the Bayes' rule using observed data, which inherently contains uncertainties. The resulting PDF is referred to as the posterior distribution. When both the prior distribution of the model parameters and the distribution of measurement error follow a Gaussian distribution, and the forward model (likelihood function) is linear, it is possible to derive a closed-form solution of the posterior PDF analytically (Tarantola, 2005). This analytical approach offers the advantage of computational efficiency. Buland and Omre (2003) developed the Bayesian linearized amplitude versus offset (AVO) inversion method, which is based on a linearized approximation of Zoeppritz equations and a convolutional seismic model. Subsequently, this method was extended to various geophysical inverse problems, including cross-borehole tomography (Hansen et al., 2006), time-lapse seismic inversion (Buland and El Ouair, 2006), controlled source electromagnetic inversion (Buland and Kolbjørnsen, 2012), rock physics inversion (Grana, 2016), and petrophysical AVO inversion (Lang and Grana, 2018). Moreover, the analytical posterior distribution can be obtained for linear inverse problems with certain simple non-Gaussian prior distributions, such as the Gaussian mixture (Grana et al., 2017) or skewed Gaussian (Rimstad and Omre, 2014) distributions.

However, in cases where the forward model is non-linear or the prior distribution is complex, obtaining an analytical solution is often infeasible. As a result, we must rely on numerical inference methods to approximate the posterior distribution. Roughly speaking, we can categorize these numerical techniques into two types: sampling and optimization. Markov Chain Monte Carlo (MCMC) is a popular sampling method that has been used in various geophysical inverse problems, for example, gravity inversion (e.g., Mosegaard and Tarantola, 1995; Wei et al., 2023), electromagnetic inversion (e.g., Ramirez et al., 2005; Ray et al., 2013; Peng et al., 2022), and seismic inversion (e.g., Hong and Sen, 2009; de Figueiredo et al., 2019; Grana et al., 2023). While MCMC is a powerful approach, it can be computationally expensive, especially for high-dimensional problems or complex models. In recent years, significant advancements in MCMC algorithms, such as Hamiltonian Monte Carlo (Neal, 2011) and stochastic Newton MCMC (Martin et al., 2019), have helped tackle some of these challenges, enabling more efficient sampling from complex posteriors in geophysical inverse problems (Fichtner and Simutė, 2018; Zhao Z. and Sen, 2021; Gebraad et al., 2020).

Optimization-based inference methods provide an attractive alternative due to their computational efficiency. Variational inference is an optimization approach that aims to optimize variational parameters of a predefined distribution that is easy to sample (e.g., the Gaussian distribution) to approximate the target distribution (Nawaz and Curtis, 2018 and 2019). Although variational methods exhibit computational efficiency and scalability to high-dimensional inverse problems, they heavily rely on the chosen of variational distributions, potentially introducing biases and yielding inaccurate solutions. A comprehensive overview of the applications of variational inference in geophysical inverse problems is provided by Zhang X. et al. (2021). Another family of optimization methods consists of sequential Monte Carlo methods, including ensemble-based methods and particle filters, in which the distribution of model is represented by an ensemble of model realizations (or particles). Liu M. and Grana (2018 and 2022) developed a stochastic seismic inversion method based on ensemble-smoother with multiple data assimilation (ES-MDA) and applied it to subsurface characterization. Yardim and Gerstoft (2012) applied particle filter and smoother to track non-volcanic tremor. However, these methods do have certain limitations. Ensemble-based methods are limited to weak Gaussian problems, while the particle filter method is not well-suited for high-dimensional inverse problems. Zhang J. et al. (2018) proposed an iterative local updating ensemble smoother that is effective to estimate model parameters with multimodal distributions but significantly increases the computational cost compared to conventional ensemble smoother method. A comprehensive review of probabilistic inversion methods for subsurface characterization is presented by Grana et al. (2022). Additionally, global stochastic optimization algorithms, such as particle swarm optimization (PSO), with model order reduction can also be employed for inverse problems with uncertainty quantification (Fernández-Martínez et al., 2010; Pallero et al., 2017; Pace et al., 2021).

Over the last few years, there has been a growing interest in integrating deep learning techniques into probabilistic inverse problems to improve computational efficiency. For example, deep neural networks for surrogate modeling (e.g., Tang M. et al., 2020; Tang H. et al., 2021; Wang N. et al., 2021) and model re-parameterization (e.g., Laloy et al., 2017; Laloy et al., 2018; Liu M. and Grana, 2020; Siahkoohi et al., 2022), estimation of relevant statistics (e.g., mean and standard deviation) (Hansen and Finlay, 2022), and physics-informed neural networks, invertible neural networks and normalizing flows for uncertainty quantification (Zhang X. and Curtis, 2021; Izzatullah et al., 2022; Zhang X. et al., 2022; Zhao X. et al., 2022; Orozco et al., 2023). Apart from neural network-based techniques, novel inference methods from machine learning have also been introduced to tackle geophysical inverse problems. Siahkoohi et al. (2023) used amortized variational inference to accelerate Bayesian seismic imaging. Nawaz et al. (2020) combined variational inference with neural networks to solve large geophysical inference problems. Furthermore, the Stein variational gradient descent (SVGD) method, introduced by Liu Q. and Wang in 2016, has gained prominence as a powerful tool for approximate Bayesian inference, particularly when dealing with complex and high-dimensional distributions. In geophysical inverse problems, SVGD has found applications in various areas, including seismic tomography (Zhang X. and Curtis, 2020a), post-stack seismic inversion (Izzatullah et al., 2023a), 2D full-waveform inversion (Zhang X. and Curtis, 2020b; Izzatullah et al., 2023b), hypocenter inversion (Smith et al., 2022), and parameter inference in hydrogeological models (Ramgraber et al., 2021). Zhang X. and Curtis (2023) extended the capabilities of SVGD by introducing a stochastic variant (sSVGD) to overcome the challenges encountered in high-dimensional inverse problems. Their method was successfully validated and it achieved promising results in 3D full-waveform inversion.

Inspired by the pioneering works mentioned above, we applied the SVGD method to geostatistical inversion for seismic subsurface characterization, with the aim of integrating all available information to maximally reduce the uncertainty of the subsurface.. To ensure that the inverted reservoir models preserve the prior geological knowledge, such as geostatistical characteristics including spatial correlation ranges and correlations between different reservoir properties, we introduced a strategy to re-parameterize the model parameters into latent features using an autoencoder (AE) neural network. This approach is referred to as SVGD-AE in the following. Compared to traditional probabilistic inversion methods, such as the ensemble-based method (Liu M. and Grana, 2018), SVGD-AE can provide more diverse posterior realizations, thus enabling a more precise quantification of model uncertainty. The accurate uncertainty quantification is crucial for accurate storage capacity estimates and reservoir simulations as well as for informed decision-making.

We applied the SVGD-AE method to the Illinois Basin - Decatur Project (IBDP), which is a large-scale CO_2 storage initiative in Decatur, Illinois, USA. The main goal of the IBDP is to investigate the injectivity, capacity and containment of the Mt. Simon Sandstone (Finley, 2014). Previous attempts at reservoir characterization of IBDP were limited to deterministic inversion methods with a simplified linear rock physics model (Couëslan et al., 2014), potentially leading to inaccurate results and lacking crucial information about uncertainty. In this study, we established a robust rock physics model for the IBDP and improved petrophysical property predictions using the SVGD-AE approach. The resulting petrophysical models with quantified uncertainty have broad implications in assessing storage capacity and managing injection-related risks at the IBDP. SVGD-AE can also be seamlessly integrated with differentiable physics-informed models for GCS monitoring (Liu M. et al., 2023), enabling the quantification of the uncertainty of the inversion predictions.

2. Methods

2.1 Bayesian Seismic Inversion

The goal of geophysical subsurface characterization is to infer subsurface properties from indirect surface measurements (e.g., seismic and electromagnetic data) with the calibration of logging data from boreholes. In mathematics, this procedure is a typical inverse problem, described as:

$$\mathbf{d}_{\mathrm{obs}} = \mathbf{F}(\mathbf{m}) + \mathbf{e}, \tag{1}$$

where $\mathbf{m}$ represents the properties of the subsurface of interest; $\mathbf{d}$ represents the geophysical data; $\mathbf{F}$ is the forward operator that links model parameters $\mathbf{m}$ with the observed data $\mathbf{d}_{\mathrm{obs}}$; and $\mathbf{e}$ is the additive error term associated with measurements. For seismic data, the forward modeling $\mathbf{F}$ consists of two steps:

$$\begin{aligned} \mathbf{m}_{\mathrm{e}} &= \mathbf{F}_{\mathrm{rpm}}(\mathbf{m}_{\mathrm{p}}), \\ \mathbf{d} &= \mathbf{F}_{\mathrm{seis}}(\mathbf{m}_{\mathrm{e}}), \end{aligned} \tag{2}$$

Where $\mathbf{F}_{\mathrm{rpm}}$ is the rock physics model bridging the petrophysical properties $\mathbf{m}_{\mathrm{p}}$ (e.g., porosity, mineral fractions, and fluid saturations) to elastic properties $\mathbf{m}_{\mathrm{e}}$ (e.g., P- and S-wave velocity and density); $\mathbf{F}_{\mathrm{seis}}$ is the operator that further maps elastic properties $\mathbf{m}_{\mathrm{e}}$ to seismic data; and $\mathbf{d}$ represents the modeled data without noise.

From the Bayesian perspective, both model parameters and observations are considered as random variables and are represented by probability distributions. The solution of the inverse problem, known as posterior distribution $\pi(\mathbf{m}) = p(\mathbf{m}|\mathbf{d}_{\mathrm{obs}})$, corresponding to Equation 1 can be described as follows:

$$\pi(\mathbf{m}) = p(\mathbf{m}|\mathbf{d}_{\mathrm{obs}}) = \frac{p(\mathbf{d}_{\mathrm{obs}}|\mathbf{m})p(\mathbf{m})}{p(\mathbf{d}_{\mathrm{obs}})}, \tag{3}$$

where $p(\mathbf{m})$ is the prior distribution of model parameters $\mathbf{m}$, representing our initial knowledge about the model parameters which is independent of the observed data $\mathbf{d}_{\mathrm{obs}}$; $p(\mathbf{d}_{\mathrm{obs}}|\mathbf{m})$ is the likelihood function, quantifying the agreement between the model predictions $\mathbf{F}(\mathbf{m})$ and the actual observation $\mathbf{d}_{\mathrm{obs}}$; and $p(\mathbf{d}_{\mathrm{obs}})$ is the marginal distribution of the data $\mathbf{d}_{\mathrm{obs}}$, which serves as a normalization constant. The Bayesian approach provides a powerful framework for estimating uncertainty in model parameters based on observed data while also incorporating prior knowledge. However, traditional inference methods encounter computational challenges due to the nonlinearity of the forward operator $\mathbf{F}$ and the high dimensionality of the model parameters $\mathbf{m}$.

2.2 SVGD for posterior inference

Variational inference is a technique used to approximate complex posterior distributions with simpler ones from a chosen family (Bishop and Nasrabadi, 2006). In practice, simple families like Gaussian or mean-field approximations are often used, but they may not accurately represent complex posteriors. To address this limitation, variational methods based on invertible transforms have been proposed. These methods employ a series of invertible transformations applied to an initial distribution and optimize their parameters using the Kullback-Leibler (KL) divergence (Kullback & Leibler, 1951) to approximate arbitrary posterior distributions more flexibly. This approach allows for better representation of complex and multimodal posteriors.

However, variational inference faces challenges, especially in high-dimensional settings, due to computational complexity and optimization difficulties. To tackle these challenges, the SVGD method (Liu Q. and Wang, 2016) uses a set of particles to represent the posterior distribution, avoiding the need to optimize the continuous distribution directly. This non-parametric approach with kernel-based gradient updates enables efficient refinement of particles, leading to improved approximation of complex posteriors and making SVGD a promising tool for Bayesian inference in diverse applications.

Let us consider a target probability distribution $\pi(\mathbf{m})$ over a variable $\mathbf{m} \in \mathbb{R}^d$ that we want to approximate. Directly sampling from or computing $\pi(\mathbf{m})$ may be difficult, so we introduce a set of particles $\{\mathbf{m}_i\}_{i=1}^{N_e}$ (where N_e is the total number of particles) with each $\mathbf{m}_i$ drawn from an initial distribution $q_0(\mathbf{m})$ that is easy to sample from, typically a Gaussian distribution or geostatistics simulation for geophysical inverse problems. The main objective of SVGD is to update the particles $\{\mathbf{m}_i\}_{i=1}^{N_e}$ such that their density moves towards that of the target distribution $\pi(\mathbf{m})$ with incremental transformations iteratively:

$$\mathbf{m}_i^{k+1} = \mathbf{m}_i^k + \epsilon \boldsymbol{\phi}_k\left(\mathbf{m}_i^k\right), \tag{4}$$

where $\mathbf{m}_i^k$ is the i^{th} particle at iteration k, ϵ is the step size (also known as the learning rate), and $\boldsymbol{\phi}_k(\cdot)$ is the perturbation direction at iteration k chosen to maximally decrease the KL divergence with the target distribution $\pi(\mathbf{m})$:

$$\boldsymbol{\phi}_k = \text{argmax}_{\boldsymbol{\phi}_k \in \mathcal{F}}\{\mathbb{D}_{KL}[\,q_k||\pi] - \mathbb{D}_{KL}[q_{[\mathbf{T}]}||\pi]\} \approx \underset{\boldsymbol{\phi}_k \in \mathcal{F}}{\text{argmax}}\{-\nabla_\epsilon \mathbb{D}_{KL}[q_{[\mathbf{T}]}||\pi]\}, \tag{5}$$

where $\mathcal{F}$ is called the Stein class of the probability distribution $\pi(\mathbf{m})$ satisfying $\lim_{|\mathbf{m}|\to\infty} \boldsymbol{\phi}(\mathbf{m})\pi(\mathbf{m}) = 0$, q_k is the updated distributions at iteration k that is represented by updated particles $\left\{\mathbf{m}_i^k\right\}_{i=1}^{N_e}$, $q_{[\mathbf{T}]}$ is the perturbed distribution of q_k by an incremental transformation $\mathbf{T}(\mathbf{m}) = \mathbf{m} + \epsilon\boldsymbol{\phi}(\mathbf{m})$ (Equation 4) and $\mathbb{D}_{KL}[\cdot\,||\,\cdot]$ is the KL divergence defined as:

$$\mathbb{D}_{KL}[q_{[\mathbf{T}]}||\pi] = \int q_{[\mathbf{T}]}(\mathbf{m}) \log \frac{q_{[\mathbf{T}]}(\mathbf{m})}{\pi(\mathbf{m})} d\mathbf{m}. \tag{6}$$

The functional derivative of KL divergence is exactly equal to the Stein discrepancy:

$$\nabla_\epsilon \mathbb{D}_{KL}[q_{[\mathbf{T}]}||\pi] = -\mathbb{E}_{\mathbf{m}\sim q_k}[\text{trace}(\boldsymbol{\mathcal{A}}_\pi[\boldsymbol{\phi}_k(\mathbf{m})])], \tag{7}$$

where $\boldsymbol{\mathcal{A}}_\pi$ is the so-called Stein operator:

$$\boldsymbol{\mathcal{A}}_\pi[\boldsymbol{\phi}(\mathbf{m})] \triangleq \boldsymbol{\phi}(\mathbf{m})\nabla_{\mathbf{m}}\log\pi(\mathbf{m}) + \nabla_{\mathbf{m}}\boldsymbol{\phi}(\mathbf{m}). \tag{8}$$

The detailed derivation of Equations 7 and 8 can be found in Text S1 of Supporting Information. Therefore, the optimization problem in Equation 5 is equivalent to

$$\boldsymbol{\phi}_k^* = \underset{\boldsymbol{\phi}_k \in \mathcal{F}}{\operatorname{argmax}} \{\mathbb{E}_{\mathbf{m}\sim q_k}[\operatorname{trace}(\boldsymbol{\mathcal{A}}_\pi[\boldsymbol{\phi}_k(\mathbf{m})])\}. \tag{9}$$

The Stein class $\mathcal{F}$ plays an important role in optimizing the kernelized divergence and approximating the target distribution $\mathcal{F}$. To make the optimization problem computationally tractable, Liu Q. and Wang (2016) proposed a kernelized Stein discrepancy by maximizing Equation 8 in the unit ball of a reproducing kernel Hilbert space (RKHS): $\mathcal{B} = \{f \in \mathcal{H}: \|f\|_{\mathcal{H}} \leq 1\}$ where $\mathcal{H}$ is a Hilbert space of functions defined on a set $\mathcal{X}$ that satisfies the reproducing property. The detailed introduction of RKHS can be found in Text S2 of Supporting Information.

With the RKHS, the closed-form solution to for the optimal perturbation direction $\boldsymbol{\phi}_k^*$ is given by:

$$\boldsymbol{\phi}_k^* \propto \mathbb{E}_{\mathbf{m}\sim q}[\boldsymbol{\mathcal{A}}_\pi[K(\mathbf{m},.)]] = \mathbb{E}_{\mathbf{m}\sim q}[K(\mathbf{m},.)\nabla_{\mathbf{m}}\log\pi(\mathbf{m}) + \nabla_{\mathbf{m}}K(\mathbf{m},.)], \tag{10}$$

where $K(\mathbf{m},\mathbf{m}_i)$ is the kernel function that measures the similarity between $\mathbf{m}$ and the i-th particle $\mathbf{m}_i$. The detailed proof can be found in Text S3 of Supporting Information. The radial basis function kernel is used in our study:

$$K(\mathbf{m},\mathbf{m}_i) = \exp(-\frac{\|\mathbf{m}-\mathbf{m}_i\|^2}{\sigma^2}), \tag{11}$$

where σ is a hyperparameter known as the bandwidth or spread of the kernel. In practice, σ is usually chosen to be $\frac{b_w M}{\sqrt{\log N_e}}$ where $M = \operatorname{Median}\{\|\mathbf{m}_i - \mathbf{m}_j\|_2^2\}$ is the median of the pairwise distance between the particles and b_w is a scaling factor.

Using this result, the update equation for each particle in the SVGD algorithm becomes:

$$\mathbf{m}_i^{k+1} = \mathbf{m}_i^k + \epsilon\mathbb{E}_{\mathbf{m}\sim\{\mathbf{m}_j\}_{j=1}^{N_e}}[K(\mathbf{m},\mathbf{m}_i^k)\nabla_{\mathbf{m}}\log\pi(\mathbf{m}) + \nabla_{\mathbf{m}}K(\mathbf{m},\mathbf{m}_i^k)]. \tag{12}$$

The term $K(\mathbf{m},\mathbf{m}_i^k)\nabla_{\mathbf{m}}\log\pi(\mathbf{m})$ serves to guide the particles $\{\mathbf{m}_j\}_{j=1}^{N_e}$ towards high probability regions of $\pi(\mathbf{m})$. Conversely, the term $\nabla_{\mathbf{m}}K(\mathbf{m},\mathbf{m}_i^k)$ encourages diversity within the set of particles $\{\mathbf{m}_j\}_{j=1}^{N_e}$, preventing the particles from collapsing into isolated modes of $\pi(\mathbf{m})$.

2.3 Autoencoder for model reparameterization

In geostatistical inversion, prior reservoir models are often generated through geostatistical simulations that incorporate prior geological knowledge, including spatial correlation ranges and correlations between different reservoir parameters. It is expected that the posterior reservoir models can accurately preserve those geostatistical characteristics after updating according to the measured data. However, due to the different sensitivity of petrophysical properties to geophysical data, the model updating process at each iteration using gradient descent methods including SVGD, might result in unphysical correlations between different petrophysical properties. For instance, porosity is highly sensitive to seismic data, leading to significant corrections at each updating iteration, whereas adjustments to other petrophysical parameters like mineral fractions and fluid saturations are generally minimal. Consequently, as illustrated in Figure 1a, the updated reservoir models often deviate from the model space constrained by the geostatistical prior knowledge.

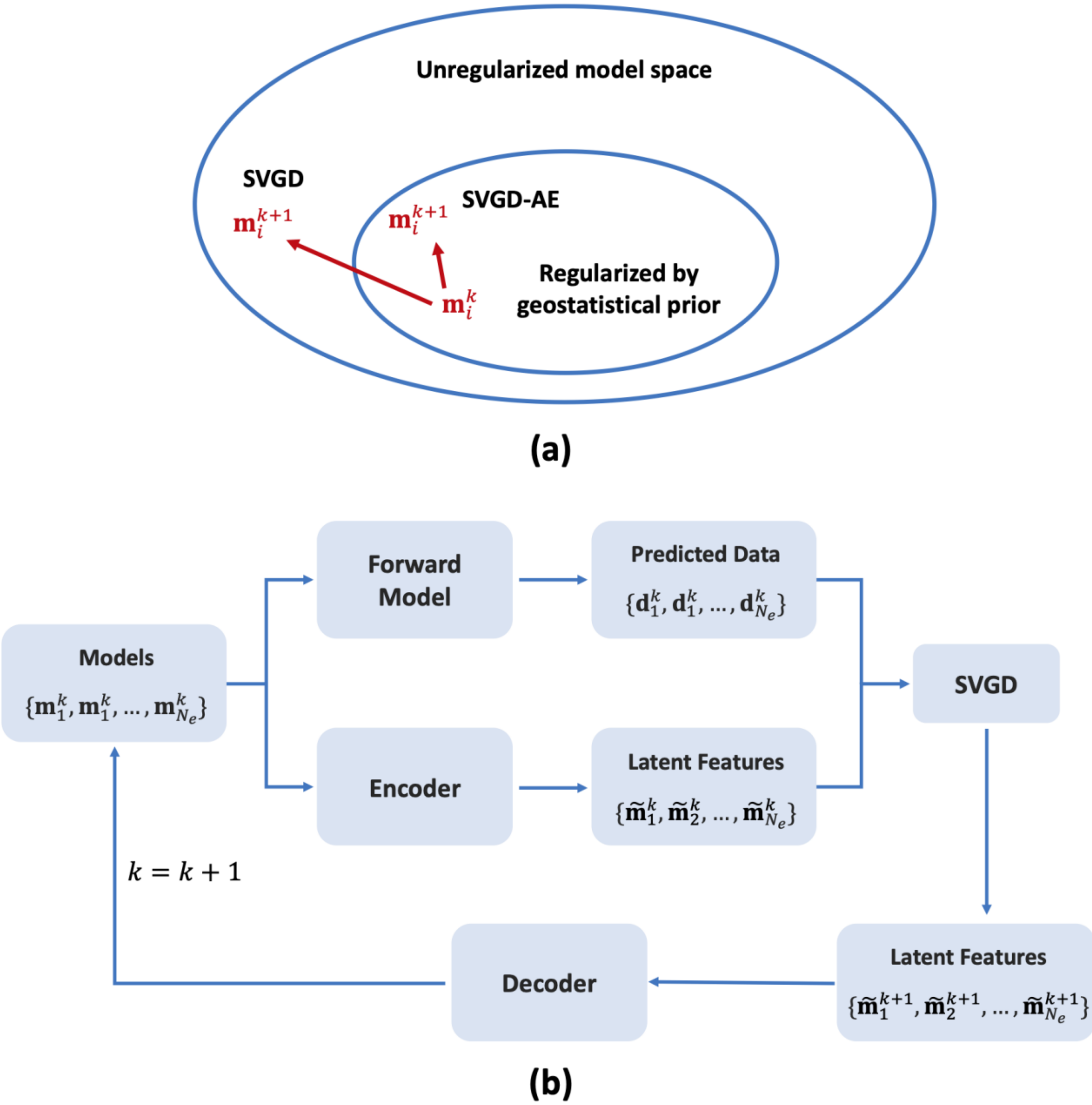

Figure 1. (a) The updated reservoir models updated by SVGD-AE consistently remain within the regularized space; (b) the workflow of SVGD-AE.

To address this issue, we propose to re-parameterize the reservoir models using an autoencoder neural network (Goodfellow et al., 2016). An autoencoder typically has two main components: an encoder $\mathcal{N}_{\mathrm{enc}}$ and a decoder $\mathcal{N}_{\mathrm{dec}}$. The encoder $\mathcal{N}_{\mathrm{enc}}$ converts model parameters $\mathbf{m}$ into latent features $\tilde{\mathbf{m}} = \mathcal{N}_{\mathrm{enc}}(\mathbf{m})$, upon which we conduct the SVGD inversion.

The decoder $\boldsymbol{\mathcal{N}}_{\text{dec}}$ transforms the updated latent features $\widetilde{\mathbf{m}}$ back into reservoir models $\mathbf{m} = \boldsymbol{\mathcal{N}}_{\text{dec}}(\widetilde{\mathbf{m}})$. AE can effectively learn information about geostatistical characteristics, including spatial features and cross-correlations, from the prior reservoir models, thus ensuring that the output reservoir models maintain these characteristics. As illustrated in Figure 1a, the updated reservoir models by SVGD-AE consistently remain within the regularized space as expected. The proposed approach is referred to as SVGD-AE, and its workflow is illustrated in Figure 1b. The complete scheme of the SVGD-AE algorithm for geostatistical inversion is described in Algorithm 1.

Algorithm 1 SVGD-AE for geophysical inverse problems

1. Define the ensemble size N_e, the number of iterations N and the step size ϵ.
2. Generate an ensemble of initial realizations $\{\mathbf{m}_i\}_{i=1}^{N_e}$ from the initial distribution $q_0(\mathbf{m})$.
3. Train an autoencoder neural network (consisting of an encoder $\boldsymbol{\mathcal{N}}_{\text{enc}}$ and decoder $\boldsymbol{\mathcal{N}}_{\text{dec}}$) using the initial realizations for model re-parametrization.
4. **For** $k = 1\ to\ N$
   - Transform model parameters into the latent space: $\widetilde{\mathbf{m}}_i^k = \boldsymbol{\mathcal{N}}_{\text{enc}}(\mathbf{m}_i^k)$
   - Obtain the gradient $\nabla_{\widetilde{\mathbf{m}}_i}\log\pi(\widetilde{\mathbf{m}}_i)$ of each prior realization $\widetilde{\mathbf{m}}_i$ through automatic differentiation.
   - Update model ensemble $\{\widetilde{\mathbf{m}}_i\}_{i=1}^{N_e}$ using $\widetilde{\mathbf{m}}_i^{k+1} = \widetilde{\mathbf{m}}_i^k + \epsilon\boldsymbol{\phi}_k^*\left(\widetilde{\mathbf{m}}_i^k\right)$ where $\boldsymbol{\phi}_k^* = \frac{1}{N_e}\sum_{j=1}^{N_e}[K\left(\widetilde{\mathbf{m}}_j^k, \widetilde{\mathbf{m}}_i^k\right)\nabla_{\widetilde{\mathbf{m}}_j^k}\log\pi\left(\widetilde{\mathbf{m}}_j^k\right) + \nabla_{\widetilde{\mathbf{m}}_j^k}K\left(\widetilde{\mathbf{m}}_j^k, \mathbf{m}_i^k\right)]$.
   - Transform the updated latent features back into the original model space: $\mathbf{m}_i^{k+1} = \boldsymbol{\mathcal{N}}_{\text{dec}}(\widetilde{\mathbf{m}}_i^{k+1})$.

End

2.4 Optimization

Let the ensemble size be denoted as N_e and the number of iterations as N. In the SVGD-AE method, it is necessary to perform the forward simulation $2N_eN$ times (the factor of 2 accounts for an additional run required to compute the gradient). In practical applications, the ensemble size is commonly set to several hundreds. The number of iterations N is significantly influenced by the chosen optimization method. Standard gradient descent typically requires a small step size and, consequently, a large number of iterations (e.g., several hundreds). In this study, we use the adaptive subgradient method (AadGrad) (Duchi et al., 2011) as the optimizer to accelerate the convergence speed. The key feature of AdaGrad is its adaptive learning rate, which dynamically adjusts the learning rate for each parameter of the model based on the historical gradients for that parameter. This adaptive mechanism is achieved by scaling the learning rates inversely proportional to the square root of the sum of squared gradients for each parameter:

$$\tilde{\epsilon}_k = \frac{\epsilon_k}{\sqrt{G_k+\tau}}, \tag{13}$$

where ϵ_k and $\tilde{\epsilon}_k$ denote the learning rates before and after scaling, respectively; G_k is the accumulated squared gradient up to iteration k, and τ is a small constant added for numerical stability.

For the proposed application, the SVGD-AE algorithm typically achieves convergence within 30 iterations using the AdaGrad optimizer. As a result, the total number of forward simulations required by SVGD-AE amounts to tens of thousands, which is comparable to ensemble-based methods and significantly smaller than the number required by MCMC methods. This makes SVGD-AE computationally efficient for large-scale inverse problems with uncertainty quantification.

The proposed approach is compared to Markov chain Monte Carlo (MCMC), particle swarm optimization (PSO), and ensemble smoother with multiple data assimilation (ES-MDA). PSO is a nature-inspired optimization algorithm that was developed to simulate the social behavior of a group of particles, often representing potential solutions to inverse problems, with uncertainty quantification. In PSO, each particle adjusts its position in a multidimensional search space based on its own experience and the experiences of its neighbors. The PSO algorithm aims to iteratively improve the positions of these particles to find the optimal or near-optimal solution to the given problem. In mathematics, the velocity and position (i.e., model parameters) updating equations for a particle in the search space are as follows:

$$\mathbf{v}_i^{k+1} = w\mathbf{v}_i^k + c_1 r_1(\mathbf{p}_i^k - \mathbf{m}_i^k) + c_2 r_2(\mathbf{p}_g^k - \mathbf{m}_i^k), \tag{14}$$

$$\mathbf{m}_i^{k+1} = \mathbf{m}_i^k + \mathbf{v}_i^{k+1}, \tag{15}$$

where $\mathbf{v}_i^k$ and $\mathbf{m}_i^k$ are the velocity and position of the i^{th} particle at iteration k; $\mathbf{p}_i^k$ is the best position found by the i^{th} particle up to iteration k (local best); $\mathbf{p}_g^k$ is the best position found by any particle in the swarm up to iteration k (global best); w is the inertia weight that controls the impact of previous velocity of the particle on the current velocity; c_1 and c_2 are acceleration coefficients representing the cognitive and social components, respectively; r_1 and r_2 are random values sampled from a uniform distribution within the range [0, 1].

ES-MDA is a widely used inversion method within geosciences, hydrology, and environmental modeling. It is a variant of the Ensemble Kalman Filter (EnKF) (Evensen, 2003) and is designed to handle the challenges associated with nonlinear and non-Gaussian problems. In mathematics, the updating equations of each particle can be expressed as follows:

$$\mathbf{m}_i^{k+1} = \mathbf{m}_i^k + \mathbf{K}\left(\tilde{\mathbf{d}}_i^k - \mathbf{d}_i^k\right), \tag{16}$$

$$\mathbf{K} = \mathbf{C}_{\mathbf{md}}^k\left(\mathbf{C}_{\mathbf{dd}}^k + \mathbf{C}_{\mathbf{d}}\right)^{-1}, \tag{17}$$

where $\mathbf{m}_i^k$ is the i^{th} particle at iteration k; $\tilde{\mathbf{d}}_i^k$ is the observed data with random perturbation according to the covariance of the noise $\mathbf{C}_{\mathbf{d}}$; $\mathbf{d}_i^k$ is the predicted data obtained from $\mathbf{m}_i^k$ through the forward operator; $\mathbf{K}$ is the so called Kalman gain matrix and is computed from the crosscovariance matrix $\mathbf{C}_{\mathbf{md}}^{k}$ between the model parameters $\mathbf{m}^{k}$ and the corresponding predicted data $\mathbf{d}^{k}$, and the covariance matrix $\mathbf{C}_{\mathbf{dd}}^{k}$ of the predicted data $\mathbf{d}^{k}$.

3. Illustrative Examples

3.1 Example 1: A simple case with multimodal posterior

The first example is a simple and low-dimensional parameter estimation problem. Its purpose is to demonstrate the efficacy and advantages of the SVGD method in addressing non-linear inverse problems with multimodal posterior distributions. The forward model for this example is defined as follows:

$$d_{\mathrm{obs}} = (m_1^2 - 1)^2 \times (m_2^2 - 1)^2 + e, \tag{18}$$

where m_1 and m_2 represent two model parameters ($\mathbf{m} = [m_1, m_2]$) and d_{obs} represents the observed data (which is a scalar) with measurement error e. We assume that $d_{\mathrm{obs}} = 0$ with $e \sim \mathcal{N}(0, 0.05^2)$ and the prior distribution of model parameters is uniform within the range $[-2,\ 2] \times [-2,\ 2]$. As depicted by the approximated distribution obtained through MCMC with 10^7 samples in Figure 2a, the posterior distribution of the model parameters exhibits four distinct modes centered at (-1, -1), (-1, 1), (1, -1) and (1, 1). We compare this MCMC posterior distribution with the posterior distribution obtained by three different methods: particle swarm optimization (PSO), ensemble smoother with multiple data assimilation (ES-MDA), and SVGD.

As shown in Figure 2b, when social information is dominant (with cognitive coefficient $c_1 = 1$ and social coefficient $c_2 = 2$), the PSO algorithm (with 200 particles and 30 iterations) concentrates exclusively on a single mode within the distribution. On the contrary, when cognitive information is dominant (with $c_1 = 1$ and $c_2 = 0$), PSO shows a higher potential to explore other modes. However, in this scenario, each particle tends to disregard information from its counterparts, resulting in the posterior particles becoming uniformly distributed among the region that cover all four modes (Figure 2c).

ES-MDA applies a shared Kalman gain matrix $\mathbf{K}$ for updating all particles within the ensemble. Hence, all particles move along in the same direction at every iteration. Consequently, ES-MDA might encounter challenges when handling posterior distributions that exhibit multiple modes. 200 prior particles are randomly drawn from a uniform distribution within the range $[-2, 2] \times [-2, 2]$. The corresponding posterior particles through 30 iterations using ES-MDA as well as the approximated posterior distribution are shown in Figure 2d. As expected, the updated posterior particles struggle to capture the multi-modal characteristic in the true distribution.

Different from ES-MDA, SVGD uses the local gradient information of individual particles to ensure diversity within the particle ensemble, as illustrated by Equation 12. In Figure 2e, the posterior distribution obtained through SVGD (where no autoencoder is used) with 30 iterations, 200 particles and the scaling factor α of 0.3 effectively capture the four modes present within the target distribution. However, the low probability regions connecting the modes are undersampled. By reducing the scaling factor α to 0.1 (i.e., by decreasing the bandwidth of the kernel function in Equation 11), the interaction among distant particles decreases. Such a smaller bandwidth allows the particles to explore local structures within the target distribution and therefore, the approximated distribution captures the low probability regions more accurately, as shown in Figure 2f. Furthermore, using more particles (i.e.,1000) further improves the results (Figure 2g); however, this improvement comes at the expense of increased computational costs. The above experiments demonstrate that SVGD outperforms PSO and ES-MDA for inverse problems with multi-modal posterior distribution.

We use the loss function (i.e., negative log likelihood) and the Wasserstein distance (Villani, 2009) between the posterior distributions at the current and previous iterations as the criteria for determining the number of iterations. In this example, SVGD converges effectively after 30 iterations using the AdaGrad optimization method. Figure 2h and 2i show the loss function and Wasserstein distance for the scenario with scaling factor of 0.1 and 200 particles.

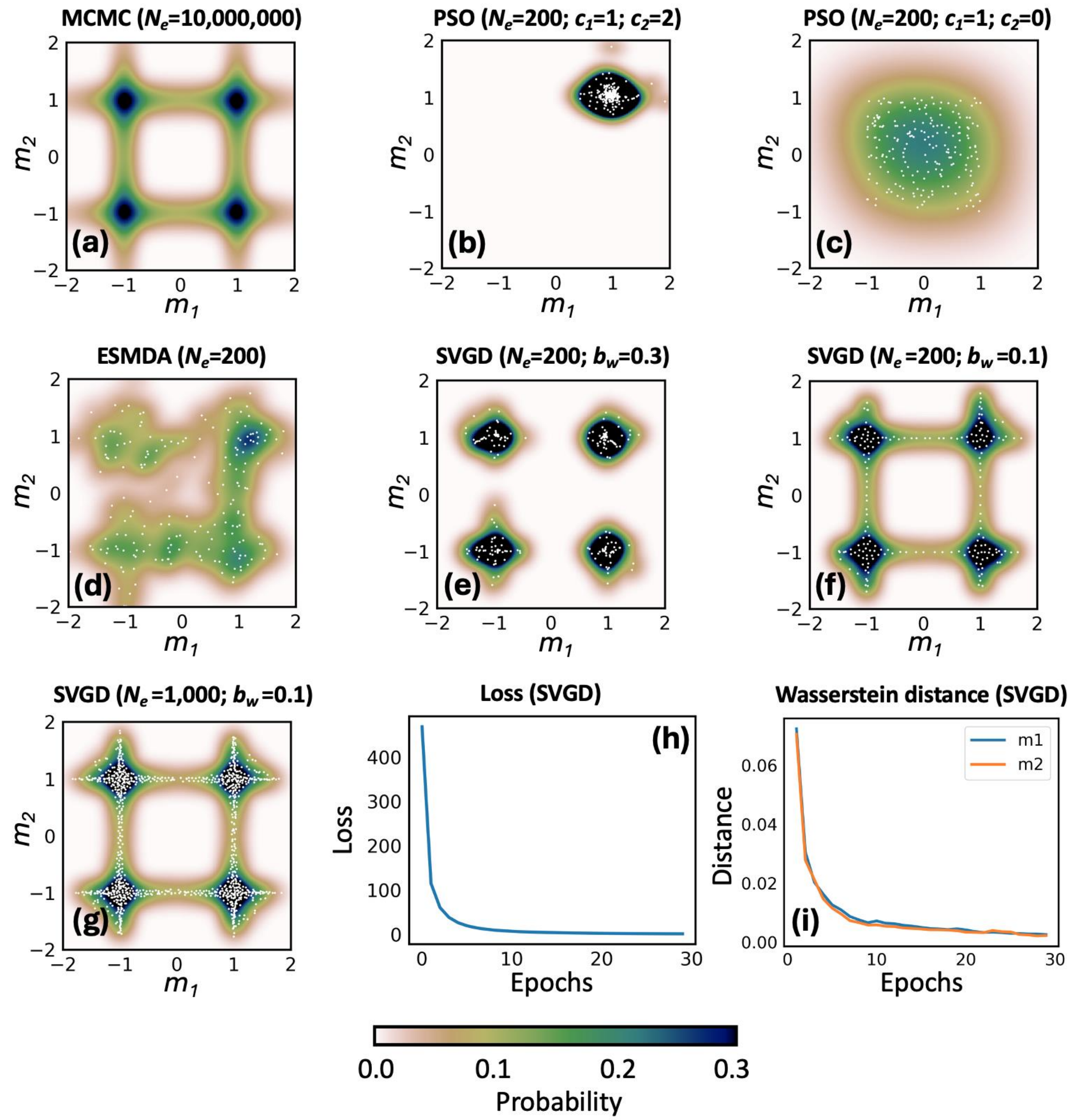

Figure 2. Posterior probability distributions approximated by (a) MCMC with 10,000,000 iterations; (b) PSO with $c_1 = 1$, $c_2 = 2$ and 200 particles; (c) PSO with $c_1 = 1$, $c_2 = 0$ and 200 particles; (d) ES-MDA with 200 particles; (e) SVGD with $b_w = 0.3$ and 200 particles; (f) SVGD with $b_w = 0.1$ and 200 particles; (g) SVGD with $b_w = 0.1$ and 1,000 particles; (h) loss function and (i) Wasserstein distance of SVGD with $b_w = 0.1$ and 200 particles over iterations. The white dots represent the posterior particles, and the posterior distributions are computed from the particles by kernel density estimation.

3.2 Example 2: A synthetic case of pre-stack AVO inversion

Although SVGD is powerful for inferring complex distributions, it often leads to unphysical correlations between reservoir properties in geostatistical inversion, as illustrated in Figure 1a. The second example aims to demonstrate the significance of the autoencoder for model re-parameterization and to validate the SVGD-AE method for geophysical inverse problems, specifically the pre-stack AVO inversion for estimating petrophysical properties. The reference petrophysical model of porosity and clay volume (Figure 3a) are generated by Gaussian co-simulation with a correlation coefficient of -0.59 and a vertical correlation length of 10 ms (Grana et al., 2022). We assume a constant water saturation of 1, which mimics the scenario before CO_2 injection consistently with the proposed real case application.

The elastic properties, including P- ($\mathbf{V}_\mathrm{P}$) and S-wave ($\mathbf{V}_\mathrm{s}$) velocities and density ($\boldsymbol{\rho}$), associated with the petrophysical model are derived using the unconsolidated sand model (Dvorkin and Nur, 1996; Mavko et al., 2020). The detailed description of the unconsolidated sand model the rock-physics parameters can be found in Text S4 and Table S1 of Supporting Information. The Shuey's three-term AVO equation (Shuey, 1985) is used to calculate the P-to-P reflection coefficients $\mathbf{R}_{PP}$ for varying incidence angles θ:

$$\mathbf{R}_{PP}(t,\theta) \approx \frac{1}{2}\left(\frac{\Delta \mathbf{V}_P}{\overline{\mathbf{V}_P}} + \frac{\Delta\boldsymbol{\rho}}{\overline{\boldsymbol{\rho}}}\right) + \left[\frac{1}{2}\frac{\Delta \mathbf{V}_p}{\overline{\mathbf{V}_p}} - 2\frac{\overline{\mathbf{V}_P}^2}{\overline{\mathbf{V}_S}^2}\left(\frac{\Delta\boldsymbol{\rho}}{\overline{\boldsymbol{\rho}}} + 2\frac{\Delta \mathbf{V}_S}{\overline{\mathbf{V}_S}}\right)\right]\sin^2\theta + \frac{1}{2}\frac{\Delta \mathbf{V}_P}{\overline{\mathbf{V}_P}}(\tan^2\theta - \sin^2\theta), \tag{19}$$

where $\Delta\mathbf{x} = \mathbf{x}(t+dt) - \mathbf{x}(t)$ ($\mathbf{x}$ denotes either $\mathbf{V}_P$, $\mathbf{V}_S$ or $\boldsymbol{\rho}$; t represents time; and dt denotes sampling rate) is the elastic difference between at the reflection interface and $\bar{\mathbf{x}} = \frac{\mathbf{x}(t+1)+\mathbf{x}(t)}{2}$ represents the average elastic properties above and below the interface. The obtained reflection coefficients are then convolved with Ricker wavelets $\mathbf{W}(\theta)$ to generate the pre-stack seismic responses $\mathbf{d}_\mathrm{seis}$:

$$\mathbf{d}_\mathrm{seis}(t,\theta) = \mathbf{W}(\theta) * \mathbf{R}_{PP}(t,\theta). \tag{20}$$

In this study, we simulate observational data by extracting seismic traces at incident angles of

12°, and 24° and 36°. The dominant frequencies of the Ricker wavelets for the three incident angels are 45, 40 and 35 Hz, respectively. These coefficients are then convolved with the respective wavelets to obtain the seismic response. To simulate measurement error, additive Gaussian noise is added to the seismic data. The signal-to-noise ratio of the so-obtained seismic data is 10. The three seismic traces in Figure 3b represent the near, mid and far stacks for the pre-stack AVO inversion. The objective of this inverse problem is to estimate the petrophysical properties (i.e., porosity and clay volume) and quantify the associated uncertainty from the band-limited and noisy seismic data.

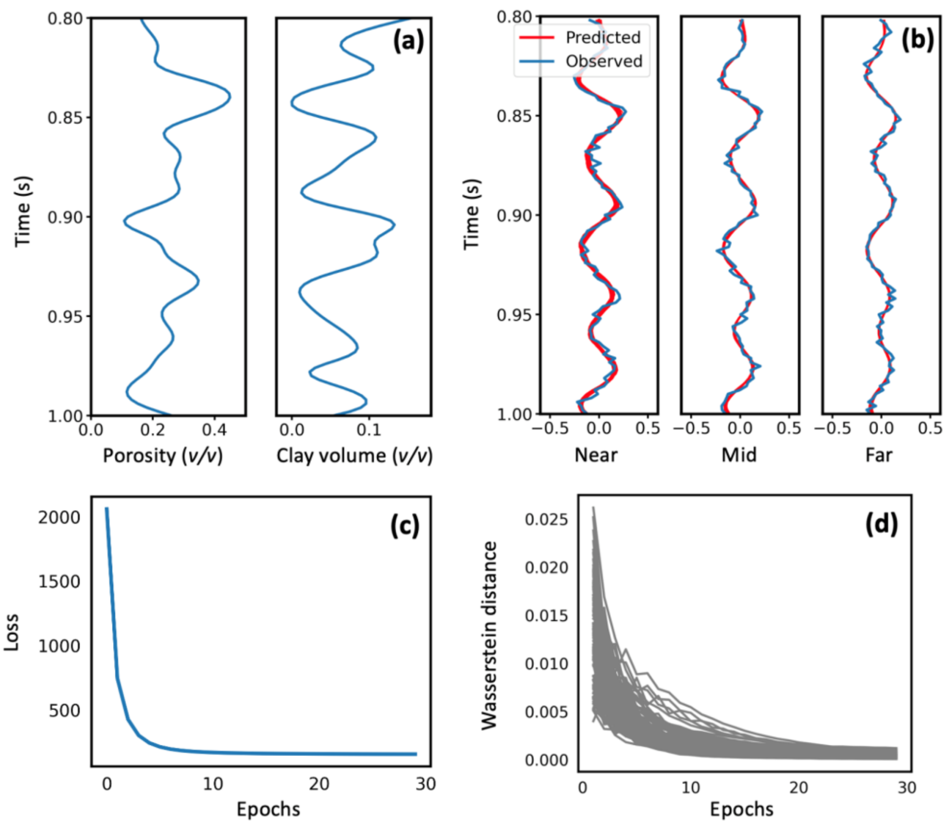

Figure 3. (a) The reference petrophysical model; (b) the actual vs. predicted seismic data; (c) the loss function and (i) the Wasserstein distance of SVGD over iterations (each gray line represents a model parameter).

The closed-form solution to this inverse problem cannot be derived analytically. Therefore, we aim at approximating the posterior distribution using MCMC, as introduced by Grana et al. (2022), which serves as the benchmark for evaluating the performance of SVGD-AE. To expediate computations and efficiently explore the model space, we use 6 parallel chains for sampling the posterior distribution. The proposed distributions of the 6 chains are correlated Gaussian distributions with vertical correlations ranging from 5 to 10 ms. Each chain is run for 10^5 iterations, with a burn-in phase of 10^4 models. Consequently, we obtain a total of 5.4×10^5 samples, and the posterior distribution approximated by MCMC is shown in Figure 4a.

Following the inversion workflow of SVGD-AE as outlined in Algorithm 1, we first generate a set of 3×10^5 prior petrophysical models with vertical correlations ranging from 5 to 10 ms. Using these prior models, we train an autoencoder neural network to transform petrophysical properties into latent features. The parameters of the autoencoder are summarized in Table 2 of Supporting Information. It is worth noting that feature maps without Rectified Linear Unit (ReLU) functions are used in the autoencoder, except for the last layer, to retain all latent features and preserve the high-frequency details in the original reservoir models. In the final layer, a customized linear activation function is employed to ensure that outputs fall within the range [0, 1]. Specifically, this customized activation function is linear between 0 and 1, assigning a value of 0 if the output is less than 0 and a value of 1 if the output exceeds 1. These values are then scaled to fit within the physical range of porosity [0.01, 0.6] and clay volume [0, 0.3]. The training time is about 1.4 minutes using one Nvidia A100 GPU. The comparison between the original reservoir models in the test set and their corresponding reconstructions by the trained autoencoder can be found in Figure S1 of Supporting Information.

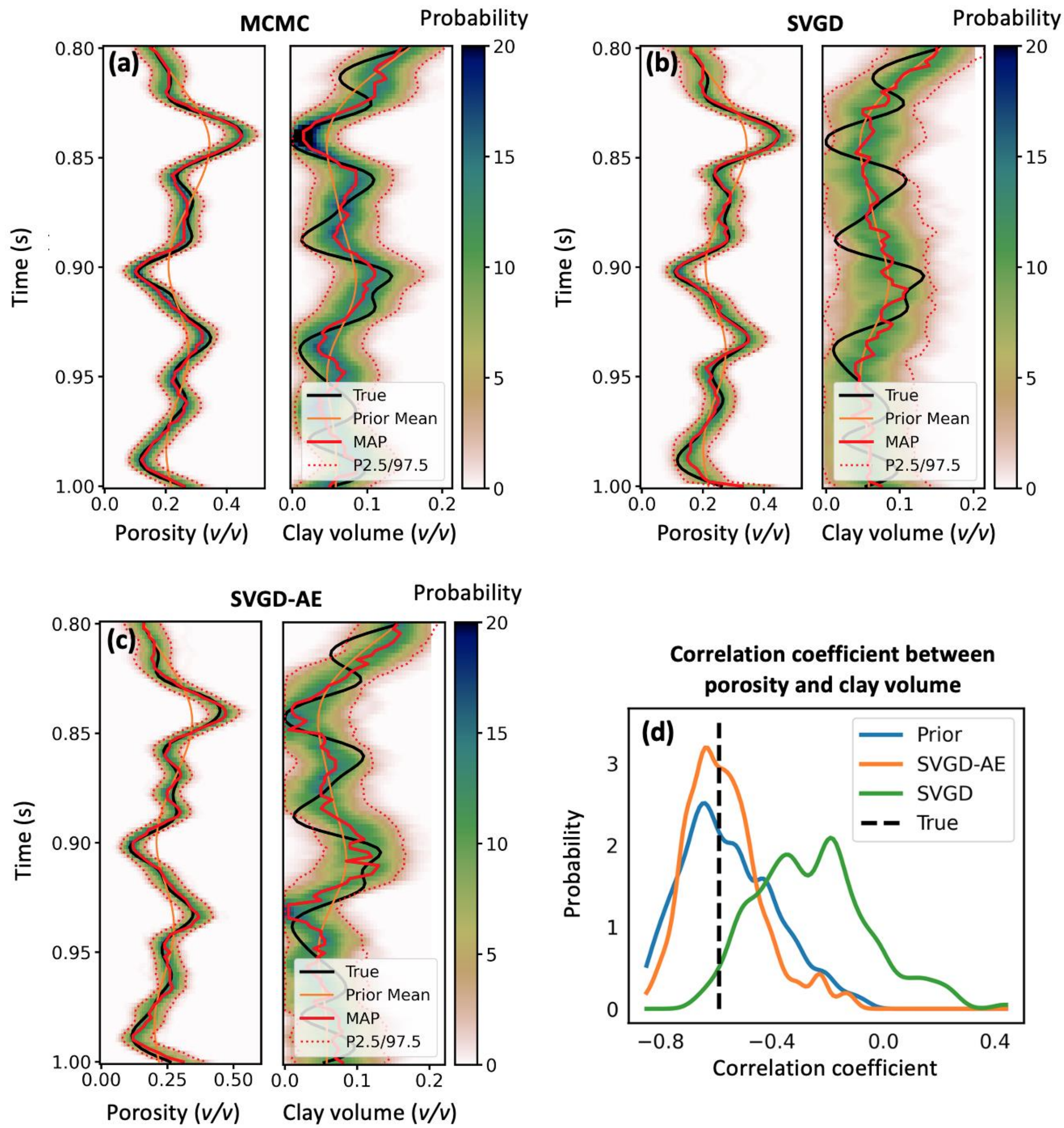

Figure 4. Petrophysical models inverted using (a) MCMC; (b) SVGD without AE; (c) SVGD-AE; (d) distributions of the correlation coefficients between porosity and clay volume for the prior realizations and the posterior realizations obtained by SVGD and SVGD-AE.

Subsequently, we randomly select 200 samples from the prior petrophysical models to form the initial ensemble and then apply the SVGD-AE method with AdaGrad as the optimizer to update the petrophysical models by assimilating the pre-stack seismic data. Convergence of the SVGD-AE algorithm is observed satisfactorily after 30 iterations (Figure 3c and 3d). As shown in Figure 4c, the posterior mean aligns well with the reference model and the associated model uncertainty is effectively quantified by the posterior realizations comparing with the results obtained by MCMC (Figure 4a). In the unconsolidated sand model, porosity is more sensitive to elastic properties than either clay volume. As expected, this results in the inverted porosity demonstrating higher accuracy and smaller uncertainty compared to the clay volume.

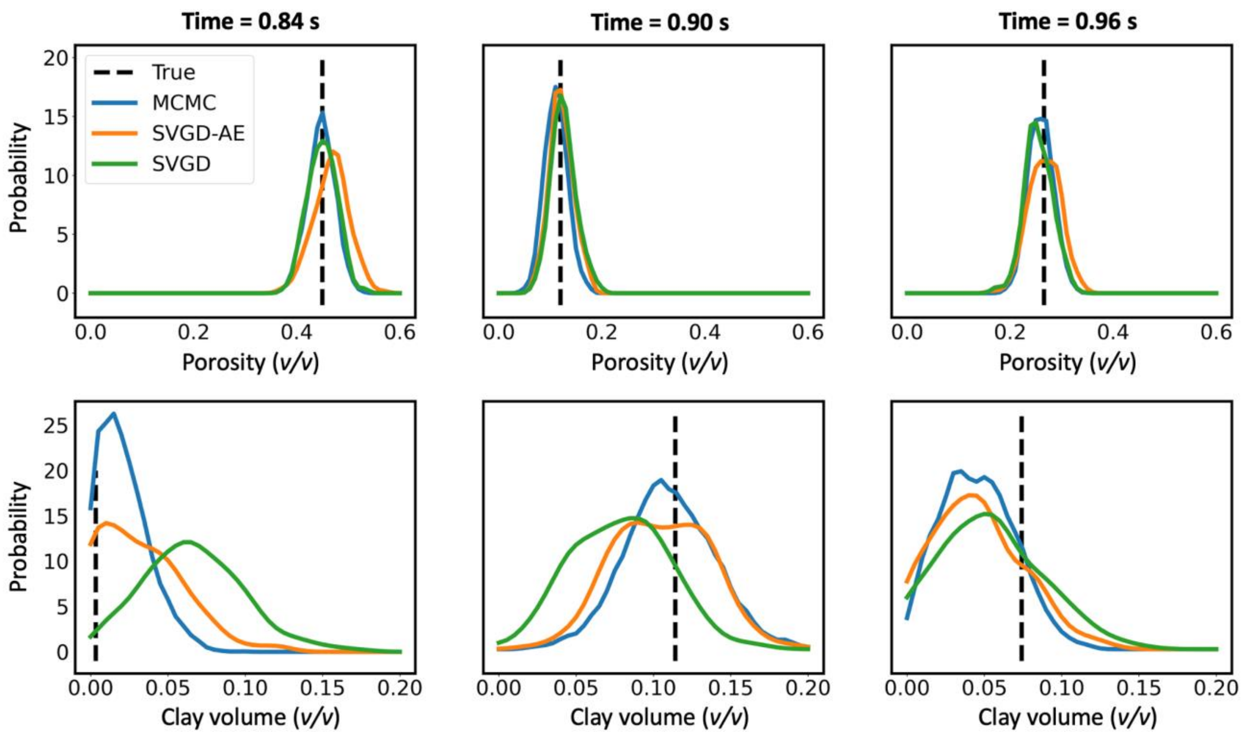

Figure 5. Marginal distributions of inverted porosity and clay volume at times 0.84, 0.9, and 0.96 s using MCMC, SVGD with and without AE.

As shown in Figure 4b, SVGD without AE accurately estimates porosity but cannot accurately recover clay volume. Moreover, Figure 4d illustrates that SVGD without AE leads to spurious correlations between porosity and clay volume, whereas SVGD-AE accurately preserves the correlations. Figure 5 presents the marginal distributions of porosity and clay volume at times 0.84, 0.9, and 0.96 s and it shows that the posterior distribution of porosity obtained by SVGD both with and without AE closely approximates that obtained by MCMC. However, for clay volume, the SVGD-AE result significantly outperforms SVGD without AE.

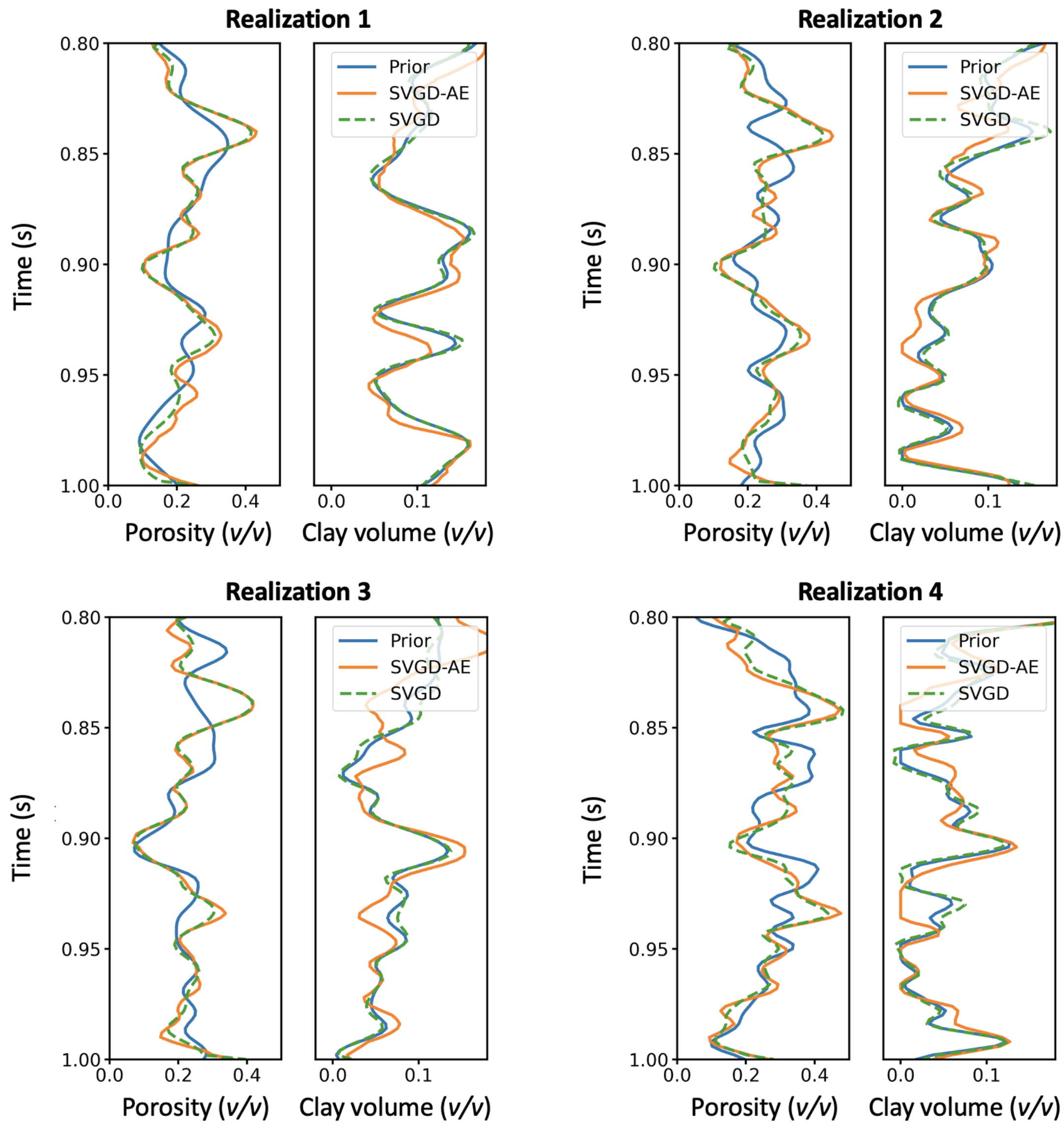

Figure 6. Four prior and posterior petrophysical realizations inverted by SVGD with and without AE.

Figure 6 shows four posterior realizations of SVGD with and without AE alongside their corresponding prior realizations. In the scenario without AE, consistent with the sensitivity to seismic data, there is minimal correction of clay volume after model updating. However, in the scenario with AE, the encoded prior information facilitates necessary corrections of clay volume, ensuring that the posterior realizations preserve geostatistical characteristics. Furthermore, while the posterior realizations of SVGD-AE differ significantly from one to another, they all generate consistent seismic responses matching the observed data, as shown in Figure 3b. This consistency indicates that all posterior realizations are valid solutions for this pre-stack AVO inverse problem. Based on our previous research (Liu M. and Grana, 2018), posterior realizations derived using the ES-MDA method share a uniform spatial trend and struggle to capture the full model space adequately. The posterior realizations typically display a uniform spatial trend with only local variability. Unlike ES-MDA, which tends to induce Gaussian posterior distributions, the SVGD-AE approach preserves the original distribution types of the prior models. Also, key geostatistical parameters of the reservoir models, such as the vertical range and sill, are effectively retained using SVGD-AE. The variety of posterior realizations provided by the SVGD method is helpful for operational decision-making as well as risk mitigation across various subsurface applications.

In Table 1, we provide a summary of the computational costs for MCMC and SVGD-AE, including the number of simulations, the number of CPU cores and the wall clock time. As the wall time can vary significantly depending on the code implementation, the number of simulations provides a reliable metric for assessing overall computational costs. In this example, SVGD-AE achieves comparable results to MCMC using only 12,000 forward simulations, whereas MCMC requires up to 300,000 forward simulations.

Table 1. A comparison of computational cost for MCMC and SVGD-AE

Method	**Number of simulations**	**CPU cores**	**Wall time (minutes)**

MCMC	300,000	6	43
SVGD-AE*	12,000	1	1

* The training of the AE incurs an additional 1.4 minutes. In real 3D applications, the training duration is negligible compared to the inversion time and can thus be ignored.

4. Application to the IBDP

In this section, we present an application of the proposed SVGD-AE method for the seismic subsurface characterization of the Illinois Basin - Decatur Project (IBDP). The IBDP project is a pioneering CO_2 storage initiative aimed at demonstrating the scalability and viability of long-term carbon dioxide sequestration in deep saline reservoirs (Finley, 2014).

4.1 Geological setting and geophysical data of the IBDP

As shown in Figure 7a, the Illinois Basin spans the Midwestern United States, covering parts of Illinois, Indiana and Kentucky. The Mount Simon (Mt. Simon) Sandstone within the basin is a thick, regional scale sandstone with a potential CO_2 storage capacity ranging from 11 to 150 billion tons (Finley, 2014). The IBDP site has drilled two injection wells (CCS1 and CCS2), two deep monitoring wells (VW1 and VW2) and various shallow wells and equipment for dedicated geophysical monitoring (Figure 7b). As revealed by the vertical injection well CCS1 (Figure 7c), the Mt. Simon formation has a depth between 1700 to 2150 m and is further divided into five lithostratigraphic subsections: Mt. Simon A through E. The CO_2 injection specifically occurred within the Lower Mt. Simon Sandstone (i.e., subsection A and B) where porosity is between 18-25% and permeability varies from 40 to 380 mD. The Mt. Simon is overlain by the Eau Claire Formation, which is a 150 m thick impermeable layer that hydraulically isolates the Mt. Simon from strata above. The Eau Claire Formation plays a vital role in preventing CO_2 leakage and guarantees secure long-term subsurface storage.

At the IBDP, three surface 3D seismic surveys were conducted to characterize the storage site and monitor CO_2 movement (Davis et al, 2019). The first 3D seismic survey in 2010 aimed to provide detailed characterization of the anticipated CO_2 plume region surrounding the CCS1 injection well. Given the potential for a more expansive CO_2 plume region than initially anticipated, the survey was expanded in 2011. The dashed red rectangle in Figure 7b outlines the coverage of the 2011 seismic survey. The extended survey in 2011 is the baseline seismic survey of the IBDP (Couëslan et al., 2014). Following the completion of the CO_2 injection, a third survey was conducted in 2015, serving as the first time-lapse monitor survey for predicting the CO_2 plumes.

In this study, we focus on the prediction of petrophysical properties with uncertainty quantification at the IBDP prior to CO_2 injection. The petrophysical models are essential for estimating CO_2 storage capacity in the area and provide baseline model for the subsequent time-lapse monitoring work. Figure 8a shows the top horizon of the Mt. Simon Sandstone in a map view with an inline crossing the wells CCS1 and VW1 and a crossline crossing the well VW2 denoted by dashed white lines. Figure 8c shows the sections of the 2011 seismic data corresponding to the dashed lines. To correlate subsurface measurements from wellbores (measured in depth) with seismic data (measured in time), we conduct a seismic-well-tie within the time window around the Mt. Simon Sandstone using wells CCS1 and CCS2. Wells VW1 and VW2 are left out to serve as blind wells for validating the inverted results. The wavelet extracted from this process is shown in Figure 8b. The synthetic seismic data produced using the extracted wavelet aligns satisfactorily with seismic traces at the well locations, indicating the reliability of our seismic-well-tie.

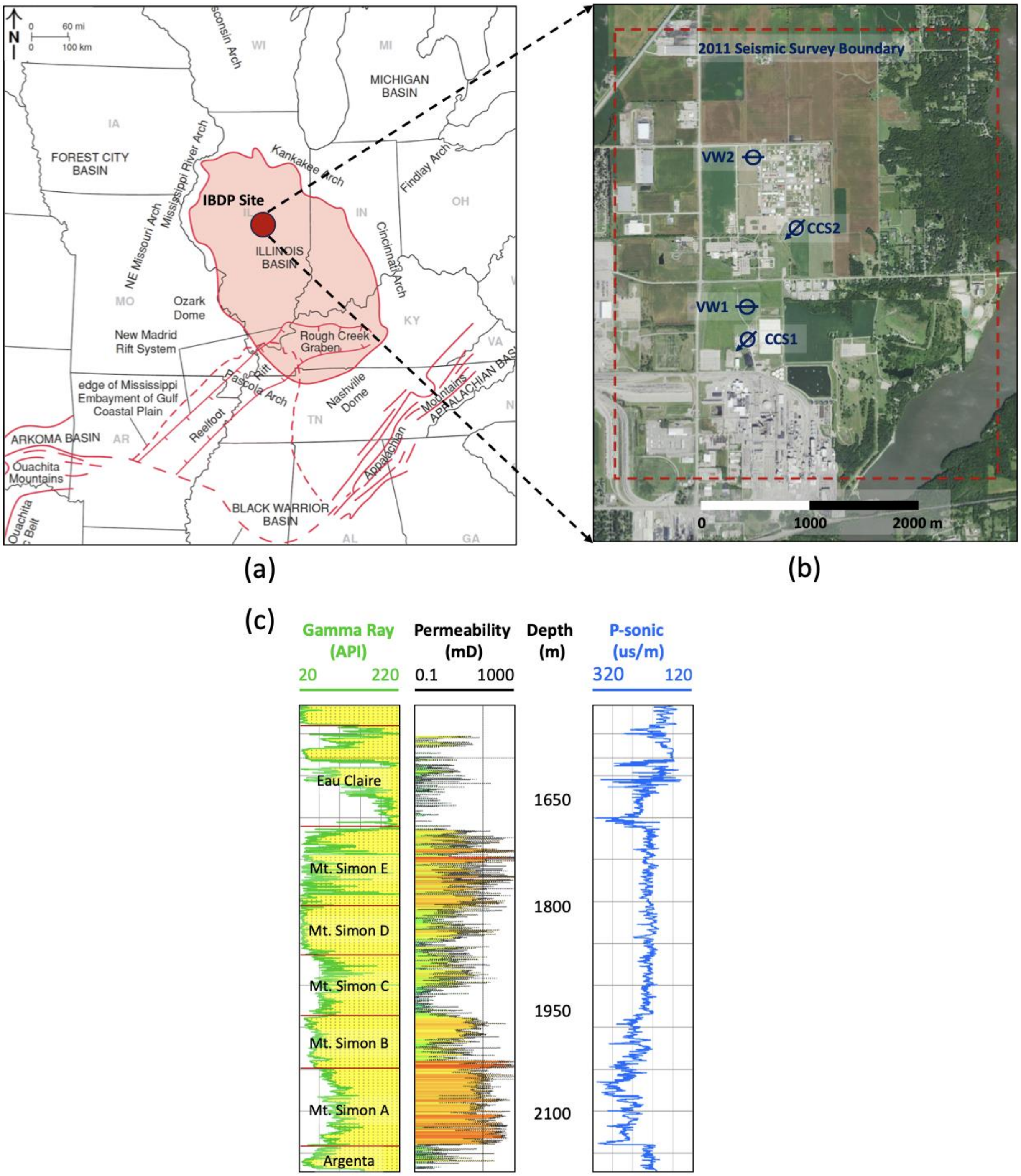

Figure 7. (a) Location of the IBDP site (red dot) and surrounding geological structures (adapted from Finley, 2014); (b) Satellite image of the IBDP site showing the location of wells (circles with an arrow denote injection wells, circles with a short line denote validation wells, and the red rectangle delineates the seismic survey boundary); (c) gamma ray, permeability and P-sonic log from Well CCS1.

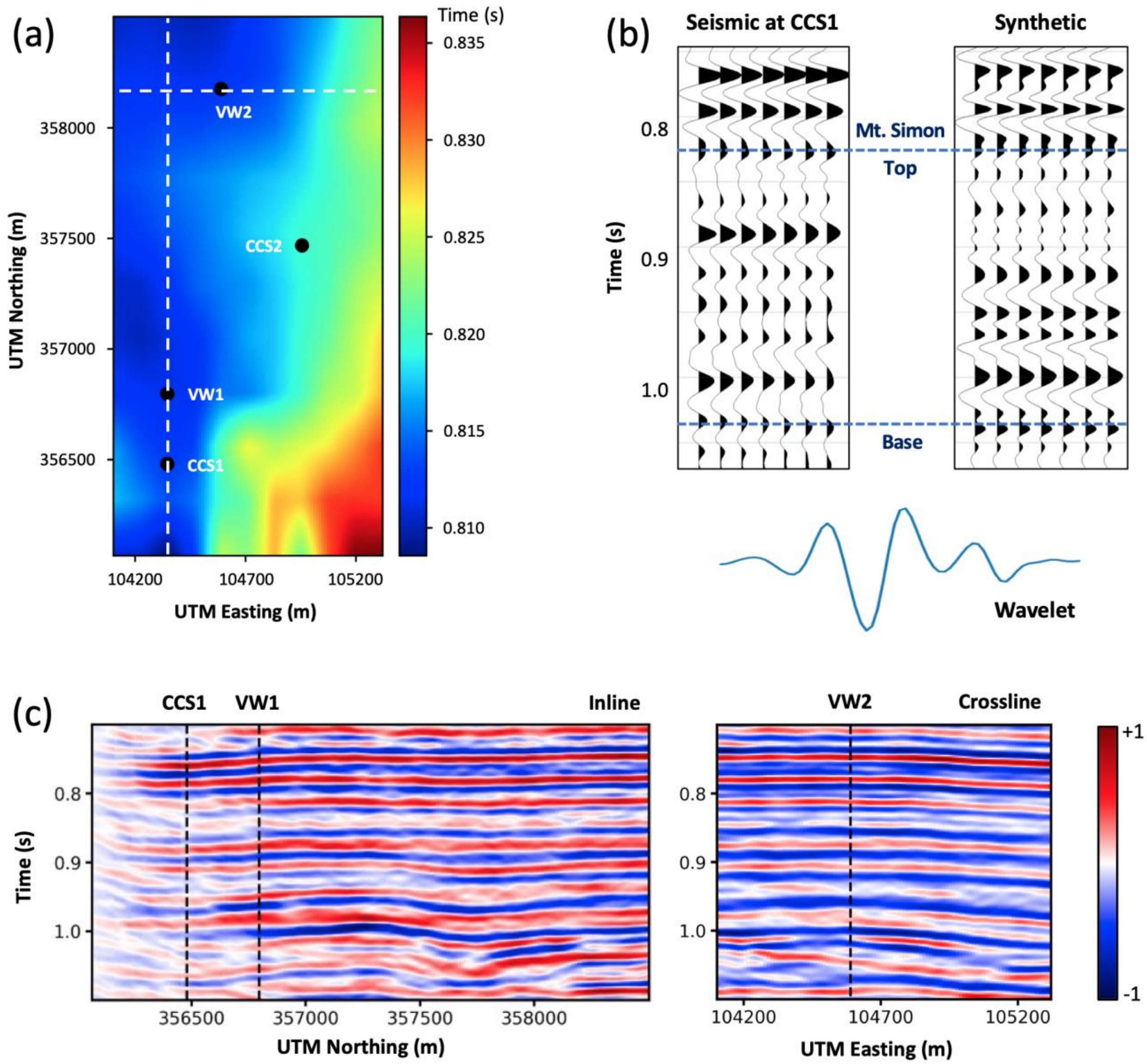

Figure 8. (a) Horizon surface from the top of the Mt. Simon Sandstone (black dots indicate well locations and dashed lines represent two sections crossing wells); (b) extracted wavelet and synthetic vs. measured seismic at Well CCS1; (c) two seismic sections corresponding to the dashed lines in (a) (the black dashed lines denote the well locations).

4.2 Rock physics modeling

While seismic data can reveal elastic properties of subsurface structures, such as velocities and density, rock physics models are essential for converting elastic properties into reservoir parameters. These parameters, including porosity, permeability, mineral fractions, and fluid saturations, are directly relevant to geologists and reservoir engineers. Figure 10 and 11 present well log data from Wells CCS1, CCS2, VW1 and VW2 within the target formation, which includes the Mt. Simon Sandstone as well as portions of the basement and caprock formations. Since Wells VW1 and VW2 are used here as blind wells for the purpose of validating inverted results, only data from CCS1 and CCS2 are used to calibrate the rock physics model.

Prior to calibrating the rock physics model, it is essential to carefully examine well logs and remove abnormal data that fall outside physical boundaries. Sandstones typically comprise various mineral components, such as quartz, feldspar, calcite, montmorillonite, illite, and kaolinite. Due to reservoir heterogeneity, these mineral fractions exhibit spatial variations, and it is difficult to obtain detailed information about these fractions. To simplify the complexity, we categorize the mineral composition into two categories: stiff and soft mineral members. The stiff mineral member comprises stiff minerals like quartz, feldspar and calcite, while the soft mineral member comprises soft minerals such as montmorillonite, illite and kaolinite. The effective physical properties of these stiff and soft mineral members are an average of their respective components, which depend on factors such as texture, cementation and diagenesis as well as reservoir pressure and temperature. In practice, these properties are estimated by fitting to the well-logs. For this work, we adopt a rock physics model known as consolidated (or stiff) sand model (Dvorkin and Nur, 1996). The detailed description of the model can be found in Text S4 of Supporting Information. Based on calibration to the log data the bulk modulus, shear modulus, and density for the stiff mineral member are taken to be 45 GPa, 44 GPa, and 2.65 g/cm^3, respectively. For the soft mineral member, these values are 21 GPa, 7 GPa, and 2.62 g/cm^3, respectively. Figures 9a-c show that the bulk modulus derived from well logs fit within the Voigt and Reuss bounds. Similarly, the P- and S-wave velocities align with the bounds defined by contact-based elastic models. Data points outside these physical limits are discarded during the subsequent rock physics modeling. From Figure 9a, the critical porosity of Mt. Simon Sandstone is determined as 0.4. The rock physics template (RPT) shown in Figure 9d provides insights into potential variations in elastic attributes with varying porosity and fluid saturations (Avseth et al., 2010). The Mt. Simon sandstones predominantly exhibit a shaly composition, as validated by the clay volume logs in Figures 10 and 11. Importantly, elastic changes with increasing CO_2 saturation remain minimal, suggesting that relying solely on time-lapse seismic data for monitoring CO_2 movement might not be effective. This observation is consistent with the 2015 time-lapse seismic data, where only subtle amplitude and waveform changes were observed post-CO_2 injection (Davis et al, 2019).

Considering the well-consolidated nature of the Mt. Simon Sandstone, we choose the consolidated sand model (Dvorkin and Nur, 1996; Mavko et al., 2020) for our rock physics modeling. In this paper, we focus on integrated site characterization for GCS, aiming to estimate static reservoir properties before CO_2 injection, wherein the reservoir is 100% water saturated. We assume that fluid properties remain constant and do not vary with reservoir temperature and pressure. However, for more reliable inversion results, it is recommended to develop a dedicated rock physics model that incorporates the effects of pressure and temperature on fluids, particularly for dynamic CO_2 monitoring (Schmitt et al., 2022).

With the refined well log data from Well CCS1 and CCS2, we optimize the rock physics parameters to ensure that the predicted elastic properties from the rock physics model align with actual measurements. Since the rock properties differ across subsections of the Mt. Simon

Sandstone, we adjust the rock physics model for each zone, accounting for variations in the bulk and shear modulus of both stiff and soft mineral assemblage. At the IBDP site, the integrated density method indicates a vertical stress gradient of 23.75 MPa/km, while formation pressure measurements reveal an in-situ hydrostatic gradient of 10.3 MPa/km within the Mt. Simon formation (Bauer et al., 2016). Thus, the resulting effective pressure gradient is 13.45 MPa/km — derived from the difference between the vertical and hydrostatic pressure gradients. We use this effective pressure gradient to calculate the varying effective stress at different depths for rock physics modeling. The water saturation is assumed to be 100% because no CO_2 was injected in 2011. Details of the calibrated rock physics parameters can be found in Table 2. Figure 10 and 11 shows the P- and S-wave velocities and density predicted by the calibrated rock physics model. The predicted elastic properties align closely with the measurements from not only Well CCS1 and CCS2, but also from blind wells, VW1 and VW2. The consistency indicates that the calibrated rock physics model is reliable and therefore can be used for the subsequent seismic inversion.

Table 2. Rock physics parameters associated with the consolidated sand model.

Parameter	**Formation**	**Value**
Bulk modulus of stiff mineral member	Mt. Simon E	45.0 GPa
	Mt. Simon D	42.0 GPa
	Mt. Simon A-C	45.0 GPa
Shear modulus of stiff mineral member	Mt. Simon E	42.0 GPa
	Mt. Simon D	40.0 GPa
	Mt. Simon A-C	44.0 GPa
Density of stiff mineral member	Mt. Simon A-E	2.65 g/cm^3
Bulk modulus of soft mineral	Mt. Simon D-E	21.0 GPa

member	Mt. Simon A-C	27.0 GPa
Shear modulus of soft mineral member	Mt. Simon D-E	7.0 GPa
	Mt. Simon A-C	12.0 GPa
Density of soft mineral member	Mt. Simon A-E	2.62 g/cm^3
Bulk modulus of brine	Mt. Simon A-E	2.5 GPa
Density of brine	Mt. Simon A-E	1.03 g/cm^3
Critical porosity	Mt. Simon A-E	0.4
Coordination number	Mt. Simon A-E	7

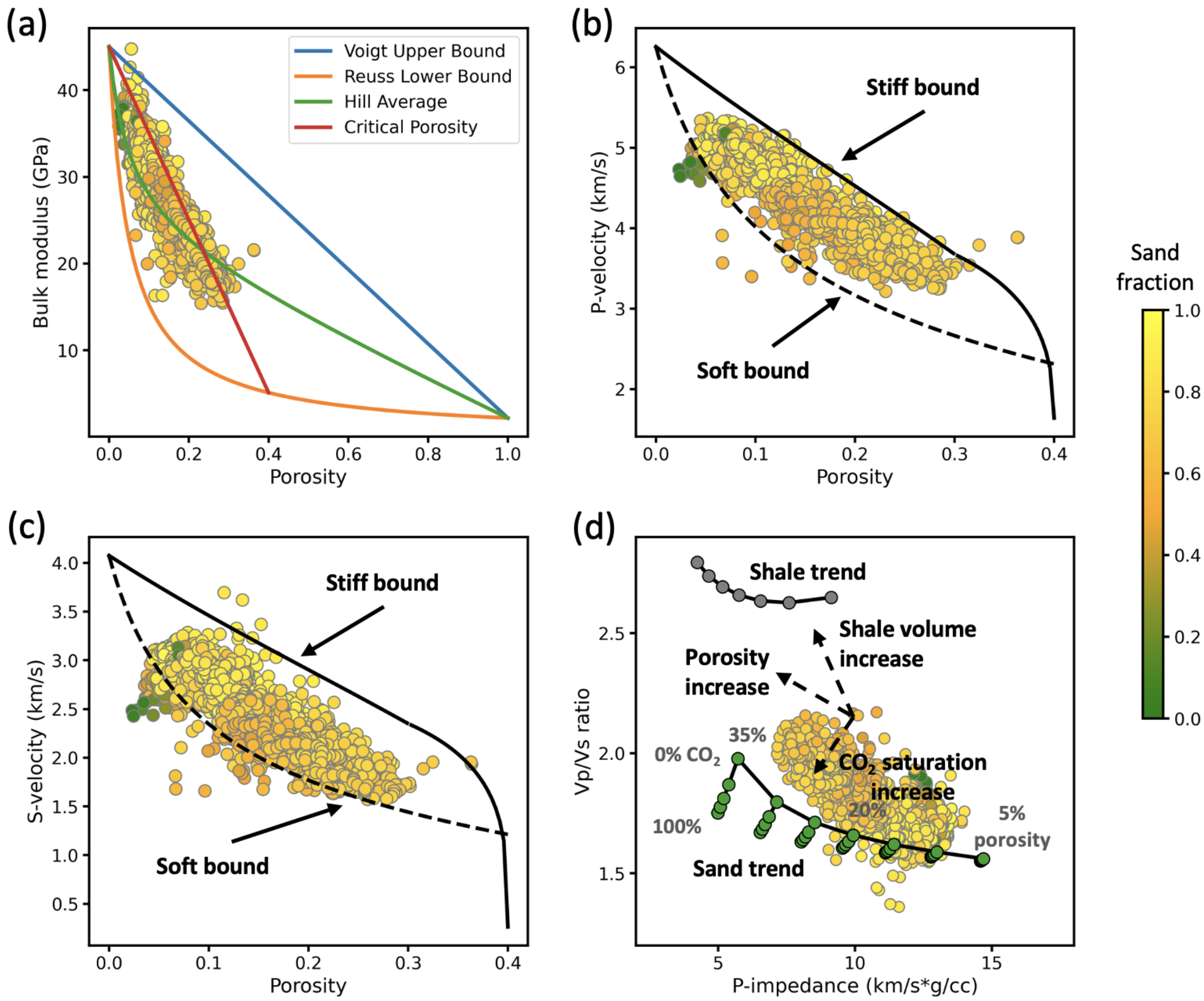

Figure 9. Rock physics analysis with well log data from Well CCS1 add CCS2 (each dot in the plots represent one data sample from the well logs): (a) Bulk modulus bounds; rock physics screening using P-velocity (b) and S-velocity (c) bounds; (d) rock physics template (the line with gray dots represents the shale trend line, and the lines with green dots represent the sand trend lines).

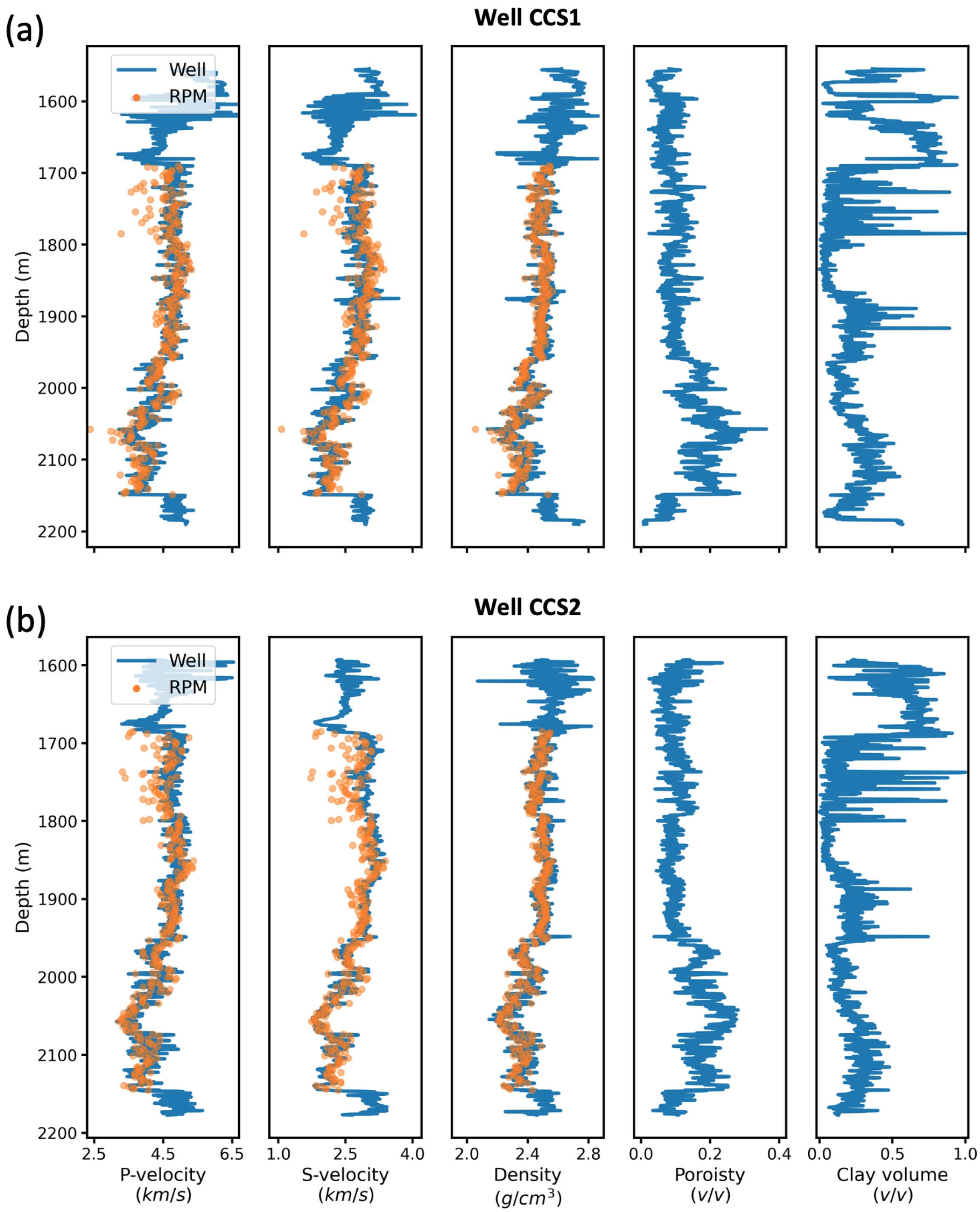

Figure 10. Actual well-log data vs. rock-physics model prediction: (a) Well CCS1; (b) Well CCS2.

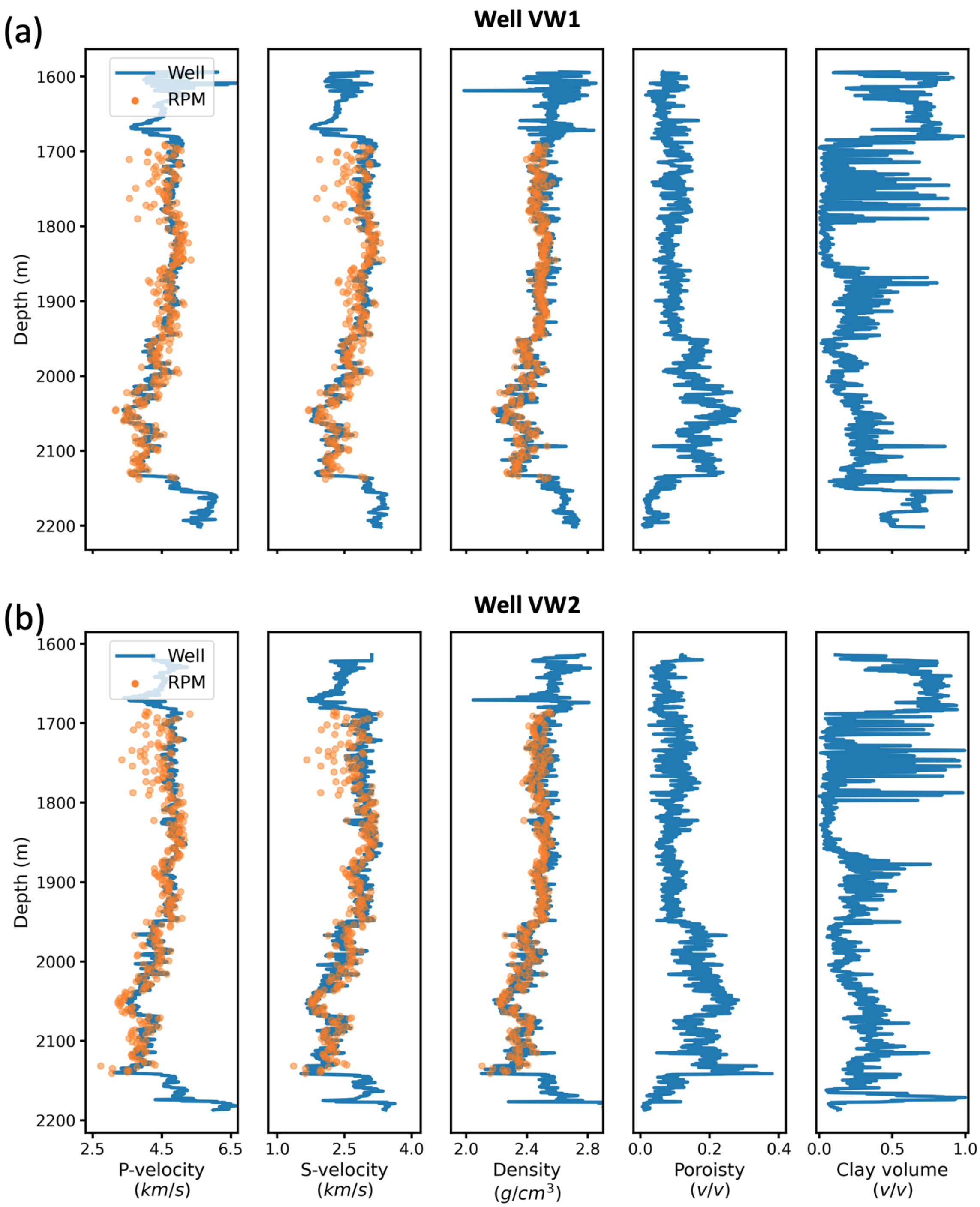

Figure 11. Actual well-log data vs. rock-physics model prediction: (a) Well VW1; (b) Well VW2.

4.3 Inversion by SVGD-AE

After seismic-well-tie and calibration of the rock physics model, we apply the proposed

SVGD-AE method to invert the post-stack seismic data. At first, we generate 200 prior petrophysical models (including porosity and clay volume) by geostatistical simulation. The vertical variogram range, determined by well logs in time domain, is 10 ms. Due to the sparse distribution of wells in the horizontal direction, which made it challenging to estimate horizontal variograms, we instead use the RMS amplitude extracted from the top horizon of the Mt. Simon Sandstone. Variograms derived from this RMS map carry more uncertainty compared to well logs. To account for such uncertainty, different horizontal ranges are used for geostatistical simulation of prior models: 120 m, 180 m, 250 m, and 310 m. The experimental variograms in easting, northing and vertical directions can be found in Figure S2 of Supporting Information.

In this study, we adopt the FFT-MA method for the generation of geostatistical simulations. The FFT-MA is an efficient approach that relies on the calculation of a filter operator based on the covariance function of interest and the convolution of the filter with a white noise (Froidevaux, 1993; de Figueiredo et al., 2020). We condition the FFT-MA simulations to available measured data at from Well CCS1 and CCS2 by using the mean and variance estimated by Kriging. Figure 12 presents the mean and standard deviation of the prior models for porosity and clay volume. Meanwhile, Figure 13 presents four simulations as the horizontal range increases from top to bottom. The prior models are then used to train an autoencoder neural network that has a similar architecture as that in the previous synthetic example. The parameters of the autoencoder are summarized in Table 3 of Supporting Information. The training time is about 3 minutes using one Nvidia A100 GPU. The comparison between the original reservoir models in the test set and their corresponding reconstructions by the trained autoencoder can be found in Figure S3 of Supporting Information.

Finally, we update the prior petrophysical models by the SVGD-AE method to assimilate the seismic data. The number of iterations is 30 in this study. Figure 14 shows the inverted results at the blind wells, VW1 and VW2. The mean of the inverted porosity has a good agreement with the well logs, while the prediction accuracy of clay volume is relatively low due to its insensitivity to seismic data. The associated model uncertainty quantified by the ensemble of posterior realizations are also shown in Figure 14, including the probability distribution as well as the percentile information of P2.5 and P97.5. The SVGD-AE approach effectively assesses uncertainty and preserves the original distribution types of the prior models.

The good match between the inverted and measured petrophysical properties at the blind wells indicates the efficacy of our proposed SVGD-AE method for seismic inversion. Thus, we extend the inversion to the entire seismic volume. The computational time is 13.4 hours using 4 CPUs. Figure 15 shows the posterior mean and standard deviation of porosity and clay volume. Figure 16 shows the four posterior realizations that correspond to the priors in Figure 13. Experimental variograms for both the prior and posterior reservoir models can be found in Figure S4 of Supplementary Information. Key geostatistical parameters of the reservoir models are effectively preserved by SVGD-AE. Specifically, the horizontal ranges observed in the posterior realizations align consistently with the variability inherent in the prior realizations.

When compared with the prior mean (Figure 12), the posterior mean (Figure 15) reveals more details after the assimilation of seismic data. Around Well CCS1, where the simulated prior reservoir models are conditioned to well log data, the uncertainty in the inverted models is minimal, while the uncertainty increases as the distance from the well grows. Additionally, the posterior mean shows that there are two distinct sandstone layers with high porosity within the Lower Mt. Simon Formation.

Figure 16 shows the four posterior realizations corresponding to the prior realizations in

Figure 13. The extent of the horizonal spreads of the posterior realizations are significantly influenced by their priors. While posterior realizations maintain the spatial features of the corresponding priors, localized updates occur ensuring diversity among the inverted realizations. In the area marked by the solid white circle in Figure 16, all four posterior realizations exhibit high-porosity sandstones with good connectivity, despite considerable differences in the corresponding prior realizations (Figure 13) in this region. This suggests that the solid white circle area represents a high-confidence optimal injection location. However, while the first realization indicates high-porosity sandstone in the region outlined by the dashed white circle, confidence in this interpretation varies among the other three realizations. Consequently, placing the injection well within the dashed white circle area poses a high risk. Hence, precise quantification of model uncertainties is crucial. Relying solely on a deterministic reservoir model for decision-making entails significant risks. Figure 17 shows the seismic responses predicted from these posterior realizations. These predictions are all consistent with the actual measurements (Figure 8c), which implies that all posterior realizations effectively explain the seismic data.

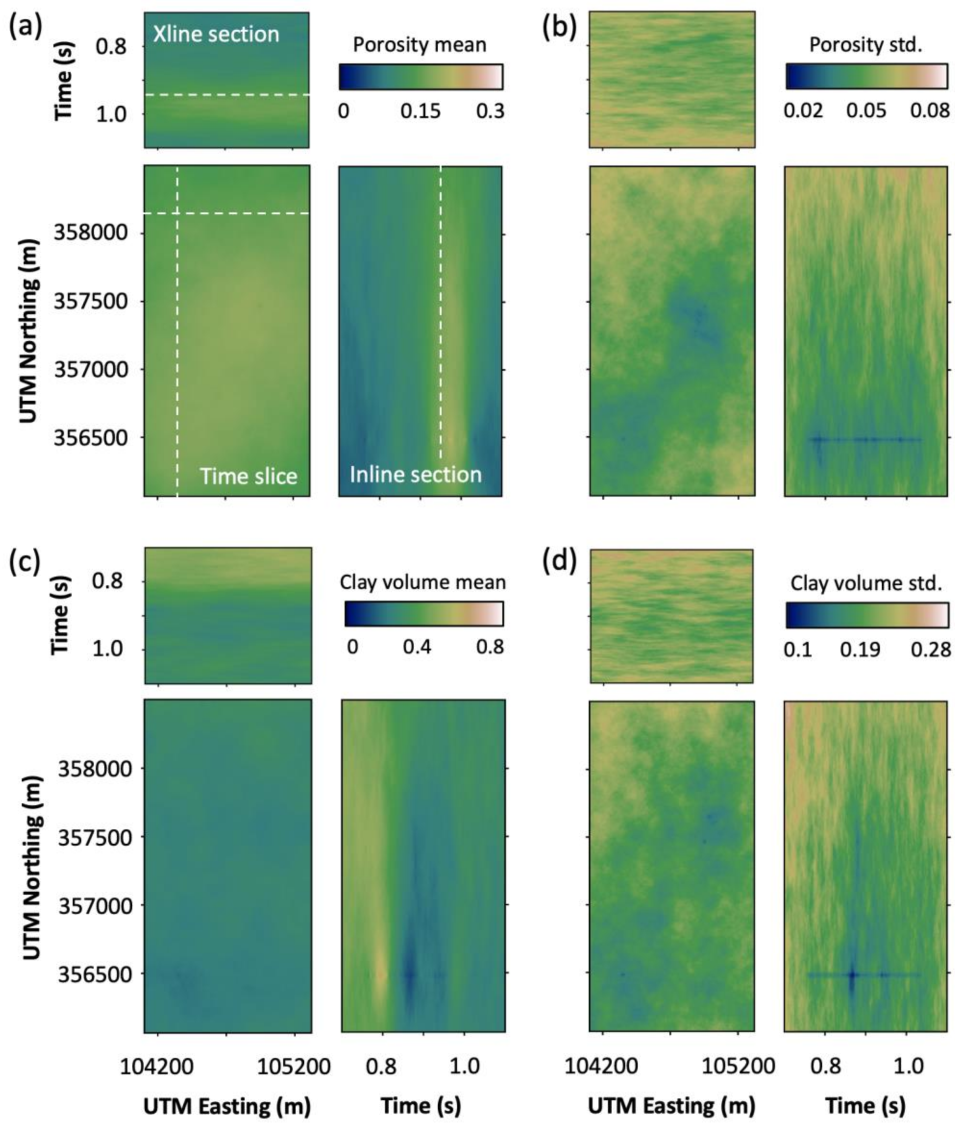

693

694 **Figure 12.** (a) Prior mean of porosity; (b) prior standard deviation of porosity; (c) prior mean of clay volume; (d)
695 prior standard deviation of clay volume. The white dashed lines represent the locations of the inline, crossline (xline)
696 and time slices.

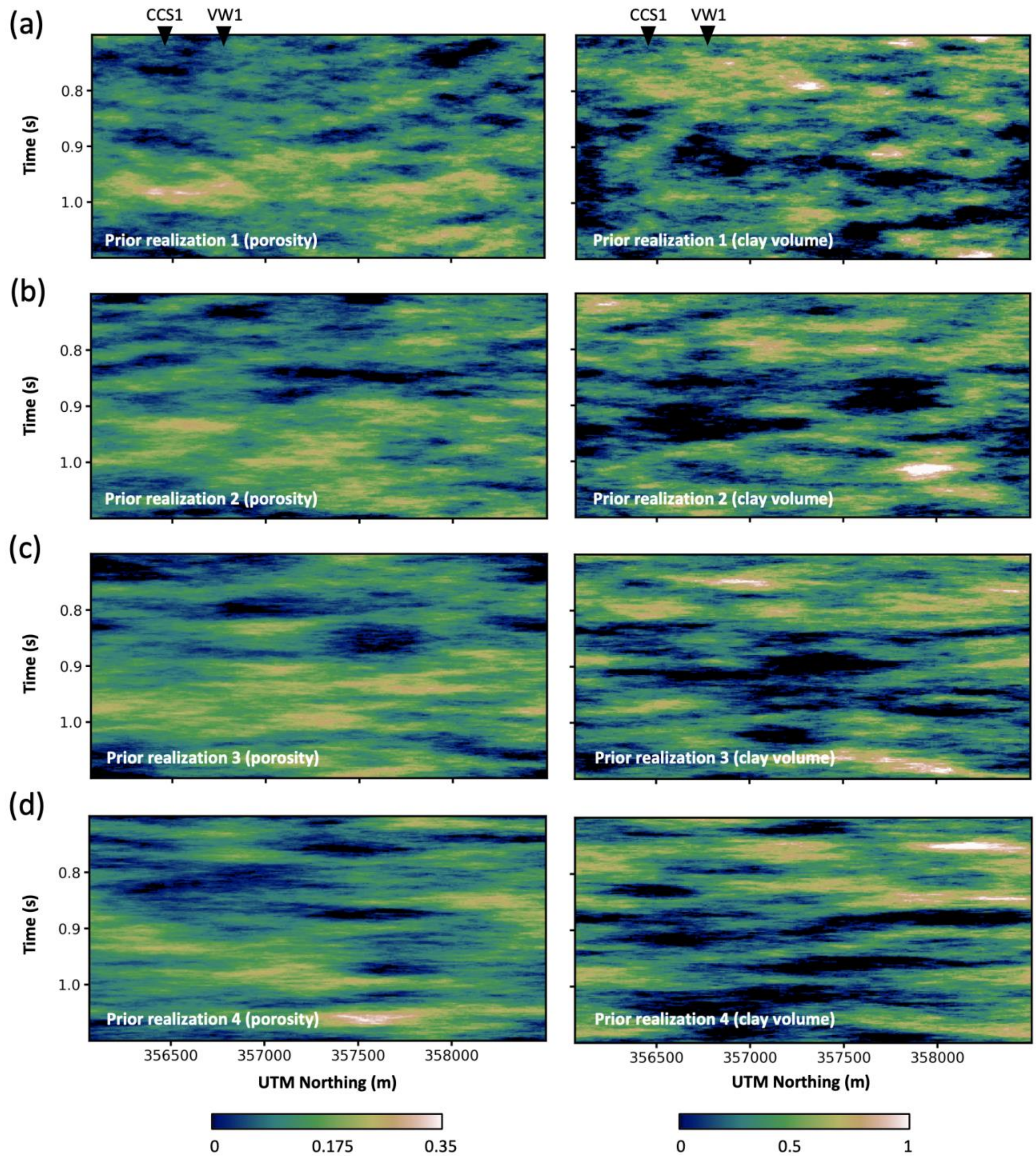

Figure 13. (a) – (d) Four prior realizations of porosity and clay volume.

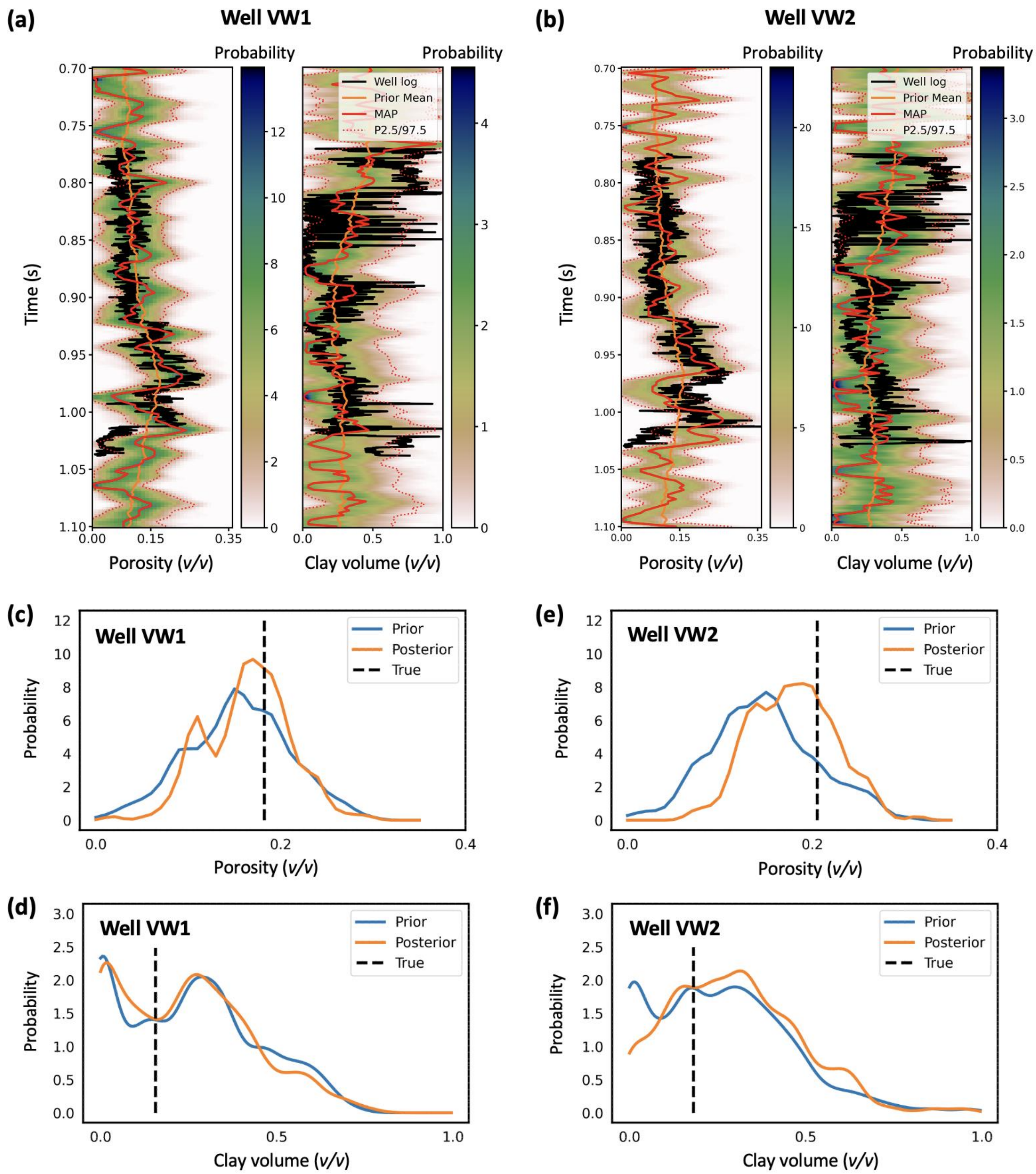

Figure 14. Validation of inversion results of SVGD-AE at blind test wells: (a) Well VW1; (b) Well VW2. Marginal distributions of inverted porosity and clay volume at times 0.95 s by SVGD-AE: (c)-(d) Well VW1; (e)-(f) Well VW2.

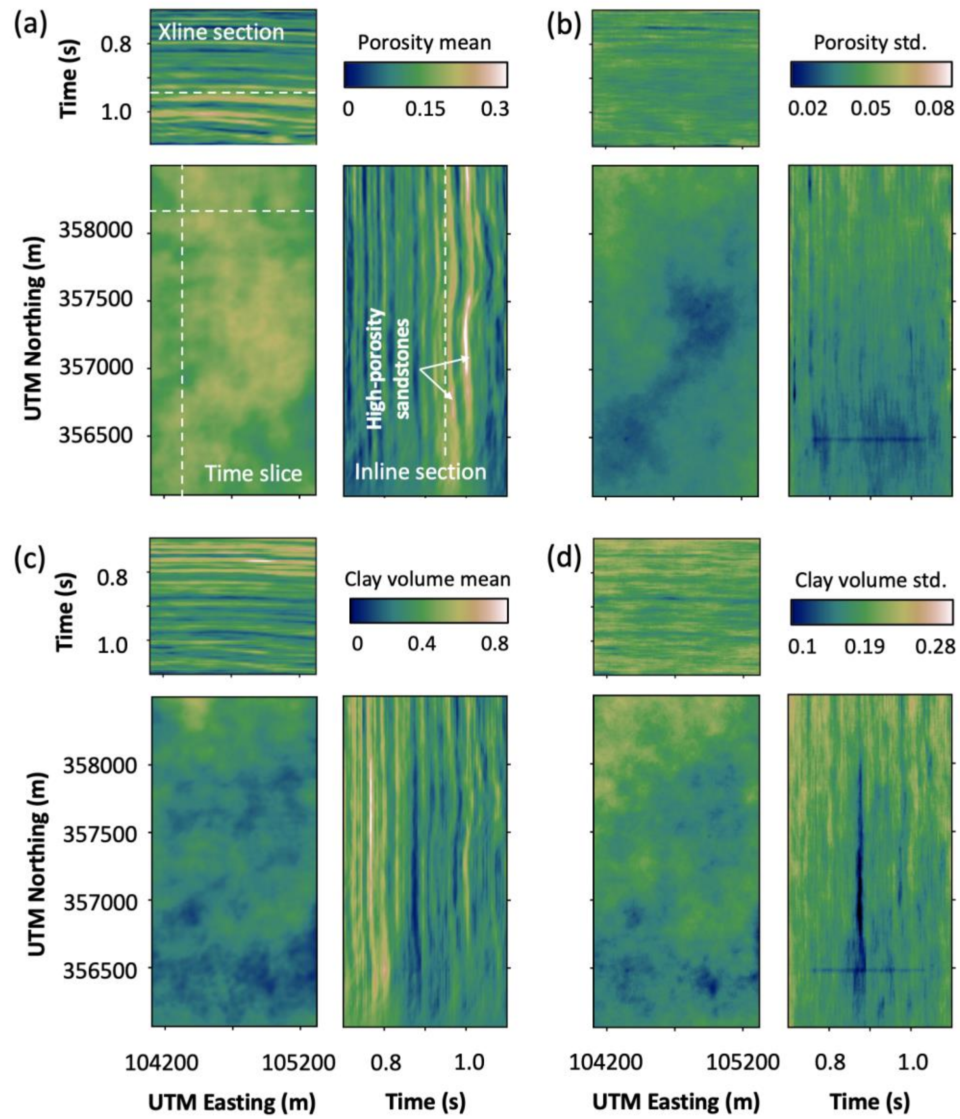

Figure 15. (a) Posterior mean of porosity; (b) posterior standard deviation of porosity; (c) posterior mean of clay volume; (d) posterior standard deviation of clay volume. The white dashed lines represent the locations of the inline, crossline (xline) and time slices.

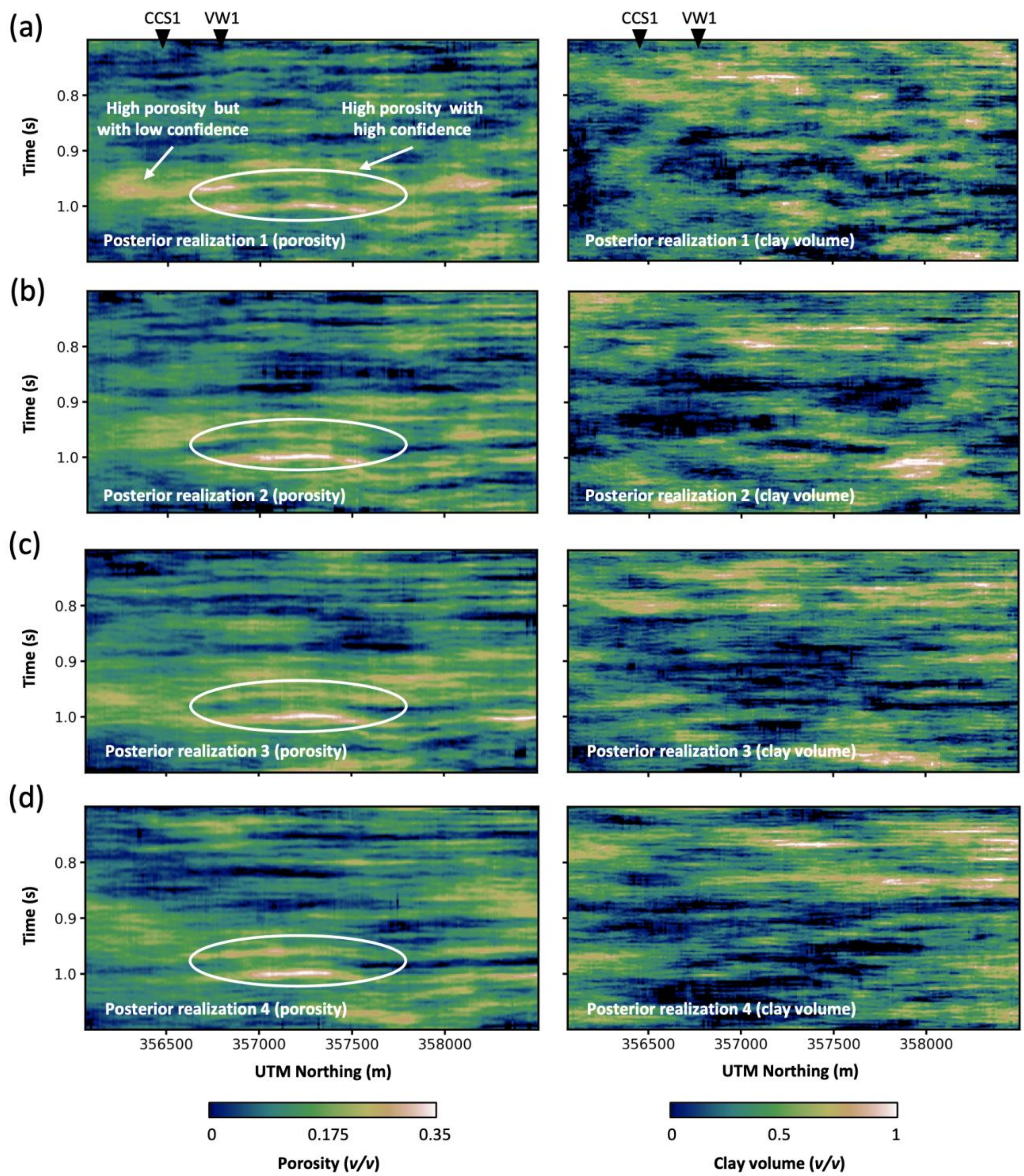

Figure 16. (a) – (d) Four posterior realizations of porosity and clay volume.

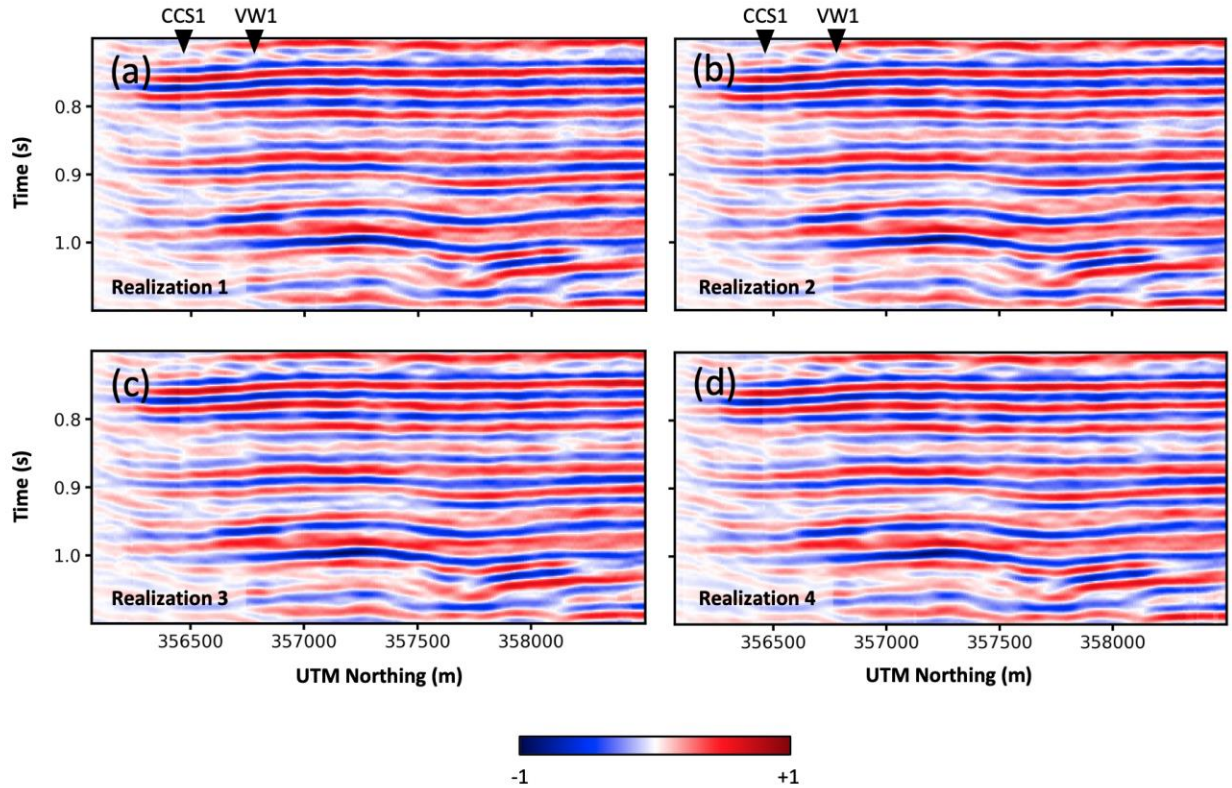

Figure 17. Predicted seismic responses from the four posterior realizations shown in Figure 13.

5. Discussions

As demonstrated in both synthetic and real examples, SVGD-AE provides an efficient method for inferring complex, high-dimensional posterior distributions. However, the initial prior distribution q_0 is one of the keys to the accuracy of quantifying the target distribution (Izzatullah et al., 2023). Initial particles (or reservoir realizations) should be easily sampled, but also must adequately span the model space. For instance, in Example 1, if prior particles are confined to a uniform distribution within $[0, 2] \times [0, 2]$ (i.e., only one quadrant of the full space $[-2, 2] \times [-2, 2]$), the posterior particles derived from SVGD will capture only a single mode of the actual distribution, neglecting other modes outside q_0. Therefore, to accurately quantify uncertainties in real geophysical inverse problems, we need to consider multiple sources of uncertainty when generating initial reservoir models via geostatistical simulations. In the application to IBDP, we focused solely on uncertainties in the horizontal variogram range. A more comprehensive approach would additionally incorporate uncertainties associated with other parameters, including the vertical range, azimuth, and orientation.

To address the issue of spurious correlations between variable reservoir parameters, we adopted an autoencoder neural network for model reparameterization. This approach seamlessly integrates with SVGD through automatic differentiation. Alternative potential solutions include principal component analysis (Vo and Durlofsky, 2015) and randomized tensor decomposition (Liu M. et al., 2022), but in those methods, we need to manually derive the required gradient terms via adjoint methods. In this study, we used a pre-trained 1D autoencoder based on initial samples obtained from geostatistical simulations and then perform the SVGD-AE inversion trace-by-trace in 1D. This approach effectively encodes our prior geostatistical knowledge into the neural network. As an alternative, amortized SVGD (Wang D. and Liu Q., 2016; Siahkoohi et al., 2023) could be used, wherein latent vectors randomly sampled from a given distribution remain constant while neural network weight parameters are updated.

To accelerate computations, we can also conduct SVGD-AE inversion section-by-section using a 2D autoencoder. Figure 18 displays four posterior realizations obtained through 2D inversion. While they are similar to those shown in Figure 16, they appear smoother and lack high-frequency details. However, SVGD-AE inversion in 2D can significantly reduce computational time. The computation time decreases from 13.6 hours using 4 CPUs for 1D inversion to 0.6 hours using one Nvidia A100 GPU.

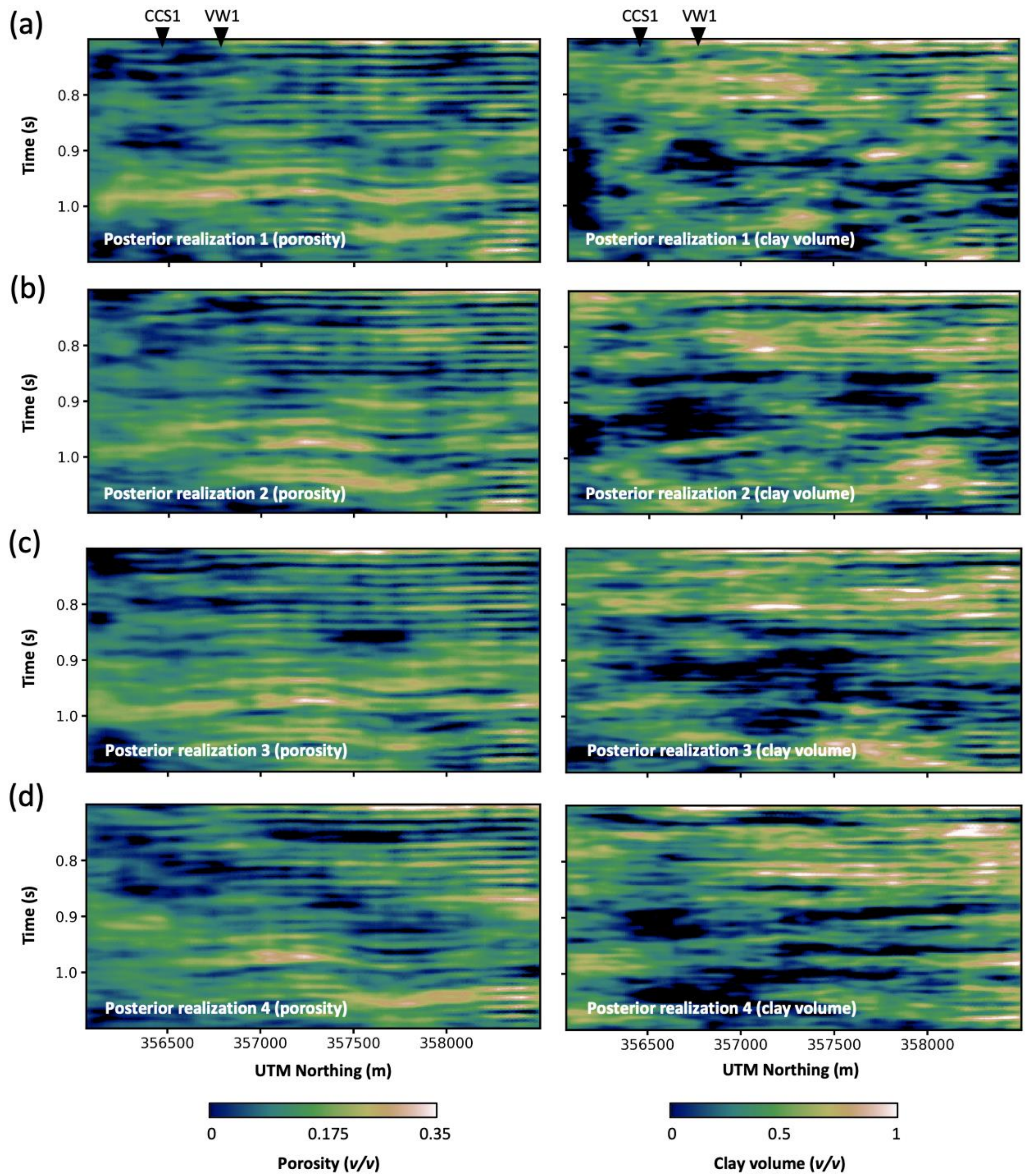

Figure 18. (a) – (d) Four posterior realizations of porosity and clay volume obtained by 2D SVGD-AE inversion.

6. Conclusion

We have developed a probabilistic inversion technique for seismic subsurface characterization in the context of geologic carbon sequestration. The proposed method, SVGD-AE, combines the Stein variational gradient descent (SVGD) approach with autoencoder neural networks for model reparameterization. SVGD effectively infers high-dimensional distributions, while the autoencoder aims to accurately preserve geostatistical characteristics of reservoir models derived from geological priors. Comparative analysis reveals that SVGD-AE outperforms conventional probabilistic methods in tackling inverse problems with multi-modal posterior distributions. To demonstrate its practicality, we have applied the SVGD-AE method in the Illinois Basin – Decatur Project. The resulting inversion results closely align with actual measurements from blind test wells. We conclude that the SVGD-AE is an efficient method for subsurface characterization with uncertainty quantification.

Data Availability Statement

The code and data used in this paper are freely available on the Mendeley Data repository (https://dx.doi.org/10.17632/b47nz2g3gb.2) (Liu M., 2023). The original IBDP dataset can be accessed publicly through the Energy Data eXchange (https://edx.netl.doe.gov/dataset/illinois-state-geological-survey-isgs-illinois-basin-decatur-project-ibdp-geological-models) (Illinois State Geological Survey, 2021).

Acknowledgements

We acknowledge the sponsors of the Stanford Center for Earth Resources Forecasting (SCERF). The authors also would like to thank Yu et al. (2023) for providing the open-source library of rock physics modeling. We also thank Editor Douglas Schmitt, as well as the two reviewers, Andrew Curtis and Tariq Alkhalifah, whose invaluable comments greatly contributed to the improvement of this paper. Additionally, we would like to acknowledge Dr. Xin Zhang for the insightful discussions on the application of SVGD in geophysical inverse problems.

.

References

- Aster, R.C., Borchers, B., & Thurber, C.H. (2018). Parameter estimation and inverse problems. *Elsevier*.
- Avseth, P., Mukerji, T., & Mavko, G. (2010). Quantitative seismic interpretation: Applying rock physics tools to reduce interpretation risk. *Cambridge University Press*.
- Bauer, R.A., Carney, M., & Finley, R.J. (2016). Overview of microseismic response to CO_2 injection into the Mt. Simon saline reservoir at the Illinois Basin-Decatur Project. *International Journal of Greenhouse Gas Control*, *54*, pp.378-388.
- Bishop, C.M., & Nasrabadi, N.M. (2006). Pattern recognition and machine learning. *New York: Springer*.
- Buland, A., & El Ouair, Y. (2006). Bayesian time-lapse inversion. *Geophysics*, *71*(3), pp.R43-R48.
- Buland, A., & Kolbjørnsen, O. (2012). Bayesian inversion of CSEM and magnetotelluric data. *Geophysics*, *77*(1), pp.E33-E42.
- Buland, A., & Omre, H. (2003). Bayesian linearized AVO inversion. *Geophysics*, *68*(1), pp.185-198.
- Couëslan, M.L., Smith, V., El-Kaseeh, G., Gilbert, J., Preece, N., Zhang, L., & Gulati, J. (2014). Development and implementation of a seismic characterization and CO_2 monitoring program for the Illinois Basin–Decatur Project. *Greenhouse Gases: Science and Technology*, *4*(5), pp.626-644.
- Davis, T.L., Landrø, M., & Wilson, M. eds. (2019). Geophysics and geosequestration. *Cambridge University Press*.
- de Figueiredo, L.P., Grana, D., Roisenberg, M., & Rodrigues, B.B. (2019). Multimodal Markov chain Monte Carlo method for nonlinear petrophysical seismic inversion. *Geophysics*, *84*(5), pp.M1-M13.
- de Figueiredo, L.P., Grana, D., & Le Ravalec, M. (2020). Revisited formulation and applications of FFT moving average. *Mathematical Geosciences*, *52*(6), pp.801-816.
- Duchi, J., Hazan, E., & Singer, Y. (2011). Adaptive subgradient methods for online learning and stochastic optimization. *Journal of machine learning research*, *12*(7).
- Dvorkin, J., & Nur, A. (1996). Elasticity of high-porosity sandstones: Theory for two North Sea data sets. *Geophysics*, *61*(5), pp.1363-1370.

- Fichtner, A., & Simutė, S. (2018). Hamiltonian Monte Carlo inversion of seismic sources in complex media. *Journal of Geophysical Research: Solid Earth, 123*(4), pp.2984-2999.
- Finley, R.J. (2014). An overview of the Illinois Basin–Decatur project. *Greenhouse Gases: Science and Technology, 4*(5), pp.571-579.
- Froidevaux, R. (1993). Probability field simulation. In Geostatistics Tróia'92: Volume 1 (pp. 73-83). Dordrecht: *Springer Netherlands*.
- Gebraad, L., Boehm, C., & Fichtner, A. (2020). Bayesian elastic full-waveform inversion using Hamiltonian Monte Carlo. *Journal of Geophysical Research: Solid Earth, 125*(3), p.e2019JB018428.
- Goodfellow, I., Bengio, Y., & Courville, A. (2016). Deep learning. *MIT press*.
- Grana, D. (2016). Bayesian linearized rock-physics inversion. *Geophysics, 81*(6), pp.D625-D641.
- Grana, D., Azevedo, L., De Figueiredo, L., Connolly, P., & Mukerji, T. (2022). Probabilistic inversion of seismic data for reservoir petrophysical characterization: Review and examples. *Geophysics, 87*(5), pp.M199-M216.
- Grana, D., de Figueiredo, L, & Mosegaard, K. (2022). Markov chain Monte Carlo for petrophysical inversion. *Geophysics, 87*(1), pp.M13-M24.
- Grana, D., de Figueiredo, L., & Mosegaard, K. (2023). Markov chain Monte Carlo for seismic facies classification. *Geophysics, 88*(3), pp.M131-M143.
- Grana, D., Fjeldstad, T., & Omre, H. (2017). Bayesian Gaussian mixture linear inversion for geophysical inverse problems. *Mathematical Geosciences, 49*, pp.493-515.
- Grana, D., Mukerji, T., & Doyen, P. (2021). Seismic reservoir modeling: Theory, examples, and algorithms. *John Wiley & Sons*.
- Hansen, T.M., & Finlay, C.C. (2022). Use of machine learning to estimate statistics of the posterior distribution in probabilistic inverse problems—An application to airborne EM data. *Journal of Geophysical Research: Solid Earth, 127*(11), p.e2022JB024703.
- Hansen, T.M., Journel, A.G., Tarantola, A., & Mosegaard, K., 2006. Linear inverse Gaussian theory and geostatistics. Geophysics, 71(6), pp.R101-R111.
- Hong, T., & Sen, M.K. (2009). A new MCMC algorithm for seismic waveform inversion and corresponding uncertainty analysis. *Geophysical Journal International, 177*(1), pp.14-32.
- Huang, L. ed. (2022). Geophysical monitoring for geologic carbon storage. *John Wiley &*

Sons.

- Illinois State Geological Survey (ISGS). (2021). Midwest Geological Sequestration Consortium (MGSC) Phase III Data Sets. [Dataset]. https://doi.org/10.18141/1854141
- Izzatullah, M., Yildirim, I.E., Waheed, U.B., & Alkhalifah, T. (2022). Laplace HypoPINN: physics-informed neural network for hypocenter localization and its predictive uncertainty. Machine Learning: Science and Technology, 3(4), p.045001.
- Izzatullah, M., Alkhalifah, T., Romero, J., Corrales, M., Luiken, N., & Ravasi, M. (2023a). Posterior sampling with CNN-based, Plug-and-Play regularization with applications to Post-Stack Seismic Inversion. *Geophysics, 89*(2), pp.1-73.
- Izzatullah, M., Ravasi, M., & Alkhalifah, T. (2023b). Physics reliable frugal uncertainty analysis for full waveform inversion. arXiv preprint arXiv:2305.07921.
- Kullback, S., & Leibler, R.A. (1951). On information and sufficiency. *The annals of mathematical statistics*, *22*(1), pp.79-86.
- Laloy, E., Hérault, R., Lee, J., Jacques, D., & Linde, N. (2017). Inversion using a new low-dimensional representation of complex binary geological media based on a deep neural network. *Advances in water resources*, *110*, pp.387-405.
- Laloy, E., Hérault, R., Jacques, D., & Linde, N. (2018). Training-image based geostatistical inversion using a spatial generative adversarial neural network. *Water Resources Research*, *54*(1), pp.381-406.
- Lang, X., & Grana, D. (2018). Bayesian linearized petrophysical AVO inversion. *Geophysics*, *83*(3), pp.M1-M13.
- Liu, M. (2023). Probabilistic Subsurface Characterization Using Stein Variational Gradient Descent with Autoencoder Neural Network. [Dataset]. https://doi.org/10.17632/b47nz2g3gb.1.
- Liu, M., & Grana, D. (2018). Stochastic nonlinear inversion of seismic data for the estimation of petroelastic properties using the ensemble smoother and data reparameterization. *Geophysics*, *83*(3), pp.M25-M39.
- Liu, M., & Grana, D. (2020). Petrophysical characterization of deep saline aquifers for CO2 storage using ensemble smoother and deep convolutional autoencoder. *Advances in Water Resources*, *142*, p.103634.
- Liu, M., Grana, D., & Mukerji, T. (2022). Randomized Tensor Decomposition for Large-Scale Data Assimilation Problems for Carbon Dioxide Sequestration. *Mathematical*

Geosciences, 54(7), pp.1139-1163.

- Liu, M., Vashisth, D., Grana, D., & Mukerji, T. (2023). Joint Inversion of Geophysical Data for Geologic Carbon Sequestration Monitoring: A Differentiable Physics-Informed Neural Network Model. *Journal of Geophysical Research: Solid Earth, 128*(3), p.e2022JB025372.
- Liu, Q., & Wang, D. (2016). Stein variational gradient descent: A general purpose Bayesian inference algorithm. *Advances in neural information processing systems, 29*.
- Martin, J., Wilcox, L.C., Burstedde, C., & Ghattas, O. (2012). A stochastic Newton MCMC method for large-scale statistical inverse problems with application to seismic inversion. *SIAM Journal on Scientific Computing, 34*(3), pp.A1460-A1487.
- Martínez, J.L.F., Gonzalo, E.G., Álvarez, J.P.F., Kuzma, H.A., & Pérez, C.O.M. (2010). PSO: A powerful algorithm to solve geophysical inverse problems: Application to a 1D-DC resistivity case. *Journal of Applied Geophysics, 71*(1), pp.13-25.
- Mavko, G., Mukerji, T., & Dvorkin, J. (2020). The rock physics handbook. *Cambridge university press*.
- Metz, B., Davidson, O., De Coninck, H.C., Loos, M., & Meyer, L. (2005). IPCC special report on carbon dioxide capture and storage. *Cambridge University Press*.
- Mosegaard, K., & Tarantola, A. (1995). Monte Carlo sampling of solutions to inverse problems. *Journal of Geophysical Research: Solid Earth, 100*(B7), pp.12431-12447.
- Nawaz, M.A., & Curtis, A. (2018). Variational Bayesian inversion (VBI) of quasi-localized seismic attributes for the spatial distribution of geological facies. *Geophysical Journal International, 214*(2), pp.845-875.
- Nawaz, M.A., & Curtis, A. (2019). Rapid discriminative variational Bayesian inversion of geophysical data for the spatial distribution of geological properties. *Journal of Geophysical Research: Solid Earth, 124*(6), pp.5867-5887.
- Nawaz, M.A., Curtis, A., Shahraeeni, M.S., & Gerea, C. (2020). Variational Bayesian inversion of seismic attributes jointly for geologic facies and petrophysical rock properties. *Geophysics, 85*(4), pp.MR213-MR233.
- Neal, R.M. (2011). MCMC using Hamiltonian dynamics. *Handbook of Markov Chain Monte Carlo, 2*(11), p.2.
- Pace, F., Santilano, A., & Godio, A. (2021). A review of geophysical modeling based on particle swarm optimization. *Surveys in Geophysics, 42*(3), pp.505-549.
- Pallero, J.L.G., Fernández-Martínez, J.L., Bonvalot, S., & Fudym, O. (2017). 3D gravity

inversion and uncertainty assessment of basement relief via particle swarm optimization. *Journal of Applied Geophysics*, *139*, pp.338-350.

- Peng, R., Han, B., Liu, Y., & Hu, X. (2022). A Julia software package for transdimensional Bayesian inversion of electromagnetic data over horizontally stratified media. *Geophysics*, *87*(5), pp.F55-F66.
- Ramgraber, M., Weatherl, R., Blumensaat, F., & Schirmer, M. (2021). Non-Gaussian Parameter Inference for Hydrogeological Models Using Stein Variational Gradient Descent. *Water Resources Research, 57*(4), p.e2020WR029339.
- Ramirez, A.L., Nitao, J.J., Hanley, W.G., Aines, R., Glaser, R.E., Sengupta, S.K., Dyer, K.M., Hickling, T.L., & Daily, W.D. (2005). Stochastic inversion of electrical resistivity changes using a Markov Chain Monte Carlo approach. *Journal of Geophysical Research: Solid Earth, 110*(B2).
- Ray, A., Alumbaugh, D.L., Hoversten, G.M., & Key, K. (2013). Robust and accelerated Bayesian inversion of marine controlled-source electromagnetic data using parallel tempering. *Geophysics*, *78*(6), pp.E271-E280.
- Rimstad, K., & Omre, H. (2014). Skew-Gaussian random fields. *Spatial Statistics*, *10*, pp.43-62.
- Scheidt, C., Li, L., & Caers, J. (2018). Quantifying uncertainty in subsurface systems (Vol. 236). *John Wiley & Sons*.
- Schmitt, D.R., Dávila, G., Yam, H., Njiekak, G., & Kofman, R. (2022). Effects of CO2 Phase State on the Seismological Properties of Porous Materials: Implications for Seismic Monitoring of Volcanic Hazards and Sequestered Carbon. *Geological Society, London, Special Publications, 528*(1), pp.SP528-2022.
- Shuey, R.T. (1985). A simplification of the Zoeppritz equations. *Geophysics, 50*(4), pp.609-614.
- Siahkoohi, A., Rizzuti, G., & Herrmann, F.J. (2022). Deep Bayesian inference for seismic imaging with tasks. *Geophysics*, *87*(5), pp.S281-S302.
- Siahkoohi, A., Rizzuti, G., Orozco, R., & Herrmann, F.J. (2023). Reliable amortized variational inference with physics-based latent distribution correction. *Geophysics, 88*(3), pp.R297-R322.
- Smith, J.D., Ross, Z.E., Azizzadenesheli, K., & Muir, J.B. (2022). HypoSVI: Hypocentre inversion with Stein variational inference and physics informed neural networks. *Geophysical Journal International*, *228*(1), pp.698-710.

- Tang, M., Liu, Y., & Durlofsky, L.J. (2020). A deep-learning-based surrogate model for data assimilation in dynamic subsurface flow problems. *Journal of Computational Physics, 413*, p.109456.
- Tang, H., Fu, P., Sherman, C.S., Zhang, J., Ju, X., Hamon, F., Azzolina, N.A., Burton-Kelly, M., & Morris, J.P. (2021). A deep learning-accelerated data assimilation and forecasting workflow for commercial-scale geologic carbon storage. *International Journal of Greenhouse Gas Control, 112*, p.103488.
- Tarantola, A. (2005). Inverse problem theory and methods for model parameter estimation. *Society for industrial and applied mathematics*.
- Villani, C. (2009). Optimal transport: old and new (Vol. 338, p. 23). *Berlin: Springe*r.
- Vo, H.X., & Durlofsky, L.J. (2015). Data assimilation and uncertainty assessment for complex geological models using a new PCA-based parameterization. *Computational Geosciences, 19*, pp.747-767.
- Wang, N., Chang, H., & Zhang, D. (2021). Deep-learning-based inverse modeling approaches: A subsurface flow example. *Journal of Geophysical Research: Solid Earth, 126*(2), p.e2020JB020549.
- Wang, D., & Liu, Q. (2016). Learning to draw samples: with application to amortized MLE for generative adversarial learning. *arXiv preprint* arXiv:1611.01722.
- Wang, H., Guo, Q., Alkhalifah, T., & Wu, Z. (2020). Regularized elastic passive equivalent source inversion with full-waveform inversion: Application to a field monitoring microseismic data set. *Geophysics, 85*(6), pp.KS207-KS219.
- Wei, X., Sun, J., & Sen, M.K. (2023). Quantifying uncertainty of salt body shapes recovered from gravity data using trans-dimensional Markov chain Monte Carlo sampling. *Geophysical Journal International, 232*(3), pp.1957-1978.
- Yardim, C., & Gerstoft, P. (2012). Sequential Bayesian techniques applied to non-volcanic tremor. *Journal of Geophysical Research: Solid Earth, 117*(B10).
- Yu, J., Mukerji, T., & Avseth, P.Å. (2023). Rockphypy: An Extensive Python Library for Rock Physics Modeling. Available at SSRN 4486364. http://dx.doi.org/10.2139/ssrn.4486364
- Zhang, J., Lin, G., Li, W., Wu, L., & Zeng, L. (2018). An iterative local updating ensemble smoother for estimation and uncertainty assessment of hydrologic model parameters with multimodal distributions. *Water Resources Research, 54*(3), pp.1716-1733.

- Zhang, X., & Curtis, A. (2020a). Seismic tomography using variational inference methods. *Journal of Geophysical Research: Solid Earth, 125*(4), p.e2019JB018589.
- Zhang, X., & Curtis, A. (2020b). Variational full-waveform inversion. *Geophysical Journal International, 222*(1), pp.406-411.
- Zhang, X., & Curtis, A. (2021). Bayesian geophysical inversion using invertible neural networks. *Journal of Geophysical Research: Solid Earth, 126*(7), p.e2021JB022320.
- Zhang, X., Hansteen, F., Curtis, A., & De Ridder, S. (2020). 1-D, 2-D, and 3-D Monte Carlo Ambient Noise Tomography Using a Dense Passive Seismic Array Installed on the North Sea Seabed. *Journal of Geophysical Research: Solid Earth, 125*(2), p.e2019JB018552.
- Zhang, X., Nawaz, M.A., Zhao, X., & Curtis, A. (2021). An introduction to variational inference in geophysical inverse problems. In Advances in Geophysics (Vol. 62, pp. 73-140). *Elsevier*.
- Zhang, X., Lomas, A., Zhou, M., Zheng, Y., & Curtis, A. (2023). 3-D Bayesian variational full waveform inversion. *Geophysical Journal International, 234*(1), pp.546-561.
- Zhao, L., Zou, C., Chen, Y., Shen, W., Wang, Y., Chen, H., & Geng, J. (2021). Fluid and lithofacies prediction based on integration of well-log data and seismic inversion: A machine-learning approach. *Geophysics, 86*(4), pp.M151-M165.
- Zhao, X., Curtis, A., & Zhang, X. (2022). Bayesian seismic tomography using normalizing flows. *Geophysical Journal International, 228*(1), pp.213-239.
- Zhao, Z., & Sen, M.K. (2021). A gradient-based Markov chain Monte Carlo method for full-waveform inversion and uncertainty analysis. *Geophysics, 86*(1), pp.R15-R30.